Guilong Li
State Key Lab of Mechanical System and Vibration,
Shanghai Jiao Tong University,
Shanghai 200240, China;
School of Mechanical Engineering,
Shanghai Jiao Tong University,
Shanghai 200240, China
e-mail: lgl52613@sjtu.edu.cn

Shichang Du[1]
State Key Lab of Mechanical System and Vibration,
Shanghai Jiao Tong University,
Shanghai 200240, China;
School of Mechanical Engineering,
Shanghai Jiao Tong University,
Shanghai 200240, China
e-mail: lovbin@sjtu.edu.cn

Bo Wang
Department of Micro/Nano Electronics,
School of Electronic Information and Electrical Engineering,
Shanghai Jiao Tong University,
Shanghai 200240, China
e-mail: wang0710@sjtu.edu.cn

Jun Lv
Faculty of Economics and Management,
East China Normal University,
Shanghai 200241, China
e-mail: jlv@dbm.ecnu.edu.cn

Yafei Deng
State Key Lab of Mechanical System and Vibration,
Shanghai Jiao Tong University,
Shanghai 200240, China;
School of Mechanical Engineering,
Shanghai Jiao Tong University,
Shanghai 200240, China
e-mail: phoenixdyf@sjtu.edu.cn

High Definition Metrology-Based Quality Improvement of Surface Texture in Face Milling of Workpieces With Discontinuous Surfaces

In face milling process, the quality of surface texture is vital for mechanical performance of workpieces. The quality of surface texture, especially for waviness, is directly affected by tool marks, a commonly observed phenomenon in face milling. However, appropriate approaches for evaluation and modeling of tool marks are absent to date. Limited to the resolution as well as the efficiency of conventional measurement instruments, the height data of tool marks is hard to be entirely obtained, leading to valuable information omission. Besides, most existing models of tool marks are established for general workpieces with regular geometry and continuous surfaces. Since the cutter-workpiece engagement mode has a significant impact on the generation of tool marks, current models could be inaccurate or invalid when dealing with workpieces with discontinuous surfaces. To overcome this shortage, a novel approach is proposed in this research, aimed at quality improvement of surface texture in face milling of workpieces with discontinuous surfaces. First, the evaluation indexes for tool marks are defined based on the recently developed high definition metrology (HDM). Second, the physical modeling of tool marks is presented, taking the face milling mechanism into account. Third, the physical-informed optimization model is developed to search for the optimal processing parameters for surface quality improvement. At last, the effectiveness of the proposed approach is verified by a face milling experiment on the engine blocks. [DOI: 10.1115/1.4051883]

Keywords: surface texture, quality improvement, high definition metrology, discontinuous surfaces, face milling, processing parameters, machining processes

1 Introduction

Surface texture, also termed as surface finish or surface topography, is the micro characteristic of a machined surface, comprising micro local deviations of the machined surface from the ideal flat plane [1–3]. Surface texture directly affects the mechanical properties of workpieces, such as contact stiffness [4], fatigue strength [5], vibration resistance [6], and sealing performance [7]. In different observation scales, the quality of surface texture can be evaluated by surface roughness and waviness, respectively [8–10].

Considerable efforts have been made to study the generation and evaluation of surface texture in various machining conditions. With reference to machining processes with defined tool geometry, Villa et al. established a mathematical model to describe the machined surface profile as an ordered sequence of tool marks [11]. Based on this model, the pattern identification procedure was developed to find out appropriate reference points on the profile [12]. Hadad and Ramezani studied the geometry of the cutting tool and subsequently established a simulation model for surface texture pattern generated in the face milling process [13]. In order to study the surface topography generation in a single-pass surface grinding process, Salisbury et al. [14] proposed a geometric-kinematic model. Furthermore, they developed a wheel surface model to be integrated with a surface grinding process model for the surface texture simulation and evaluation [15]. Baek et al. [16] proposed a physical model to analyze the effects of the insert runout errors and the variation of the feed rate on the surface texture in a face milling operation. In consideration of the effects of varying dynamics, Kiss et al. [17] proposed a finite element method-based model to present surface error calculations and stability conditions for milling operations in case of flexible workpieces. Shen et al. [18] established a neural network prediction model for the dynamic performance of the machine tool joint surface, and the influence of surface texture on the dynamic performance of joint surface was investigated. Batsch [19] developed a mathematical model of the honing process for helical gears with external teeth, aimed at obtaining the honing tool profile for machining gears with profile modifications. Most of the published research works have been verified by experimental cases based on traditional measurement equipment, such as the coordinate measurement

[1]Corresponding author.
Manuscript received December 26, 2020; final manuscript received July 18, 2021; published online August 5, 2021. Assoc. Editor: Laine Mears.

machine (CMM). However, limited to the sampling density of CMM, some valuable information of the surface texture would be inevitably missed.

In recent years, a laser holographic interferometry based noncontact measurement technology, called high definition metrology (HDM), has been increasingly concerned about by scholars [20–22]. Comparing with CMM, the major advantage of HDM lies in efficiency as well as sampling density [23,24]. A three-dimensional (3D) height map of an entire surface with relatively large area and complex geometry, consisting of millions of data points, can be generated within seconds by utilizing HDM [25]. When dealing with surface texture measurement, HDM is much more effective and efficient than conventional measurement methods. More profound and valuable information about the machining process could be revealed by reasonable analysis based on the high-resolution point cloud data provided by HDM, which is vital for surface quality control and improvement. Therefore, in this research, the HDM technology is utilized for surface texture measurement and characteristic evaluation due to its advanced measurement precision and speed over the conventional metrologies.

As one of the main components of surface texture, the periodic tool marks are commonly observed during milling and honing processes, containing huge information about the manufacturing processes to be mined. As for face milling process, tool marks are synthetically induced by the engagement mode of workpieces and cutting inserts, the tool conditions (including tool wear and insert runout), and the relative vibration of the tool and the workpiece. In practical face milling process within the computer numerical control (CNC) machine, the spindle can be slightly tilted with a small inclination (generally amounting to between 0.1 mm and 0.3 mm over a length of 1000 mm) in the direction of the feed, leading to imperfect parallelism between the disc milling cutter and the workpiece surface. The spindle tilt avoids the back-cutting effect and consequently reducing additional flank wear of the inserts, which is helpful for tool life prolonging. The dynamic performance of machining system is also affected by spindle status [26,27], which means it is necessary to take into account the chatter stability when dealing with cases of spindle tilt. Meanwhile, the engagement mode of workpiece and cutting tool is changed due to spindle tilt, resulting in surface texture with different tool marks. For quality evaluation and improvement of a face milled surface, HDM is indispensable for measuring the characteristics of tool marks. According to different inclinations adopted by the spindle in the face milling process, three typical kinds of surface texture with tool marks will remain on the machined surface of the workpiece, as shown in Fig. 1.

The advantages and disadvantages of these three kinds of spindle inclination are given by Table 1. Limited to the research scope, this research is mainly focused on the surface texture with unidirectional tool marks induced by positive inclination of spindle in face milling processes. Of note is that the concave form of the machined surface is induced by not only the spindle tilt, but also the cutting forces, fixturing, and several other factors. Herein, since the adopted inclination is quite slight, the spindle tilt is not the major contributing factor. Besides, the influence of form accuracy on surface quality evaluation can be basically removed by proper filtering processing.

The characteristics of surface texture, especially the waviness of the machined surface, will be significantly affected by the topography of tool marks, which is vital for the service performance of the workpiece. Based on HDM data, Yin et al. [28] proposed an improved approach to avoid over-segmentation when facing segmentation of surfaces with tool marks. The successfully partitioned subsurfaces with tool marks would make great contribution to the accurate prediction of sealing performance. By using the 3D surface topography measured by HDM as an indicator, Shao et al. [29] developed a model to monitor the leakage in static sealing interface. Aimed at surface variation modeling by utilizing both high resolution data from HDM and low resolution data from CMM, Ren and Wang [30] proposed a transfer learning framework for fusing multiresolution spatially nonstationary data. These researches reviewed above could provide reasonable prediction and monitoring models based on HDM measured surface texture, yet physical modeling aimed at the evaluation and generation of surface texture consisting of tool marks for workpieces with discontinuous surfaces are still relatively rare.

Workpiece geometry has been increasingly complex with the rapid development of manufacturing industry [31]. For example, the four-cylinder engine block is a typical workpiece with discontinuous surfaces, as depicted in Fig. 2. Four-cylinder bores and multiple minor holes are distributed on the top surface of the engine block, aggravating the complexity of workpiece geometry, and consequently leading to discontinuous cutter-workpiece engagement. Since the surface texture with tool marks is significantly affected by the vibration characteristics of the machining system, which is dependent on the cutter-workpiece engagement mode [32–34], it is necessary to take the face milling mechanism into consideration for more effective optimization of processing parameters.

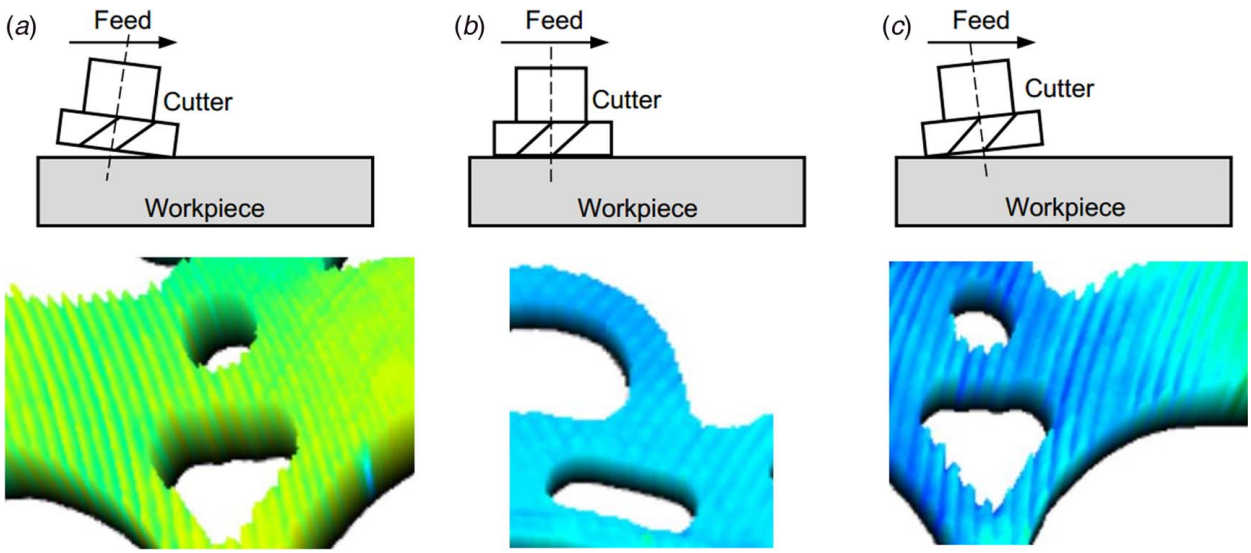

Fig. 1 Typical surface texture with different kinds of tool marks: (*a*) unidirectional tool marks caused by positive inclination of spindle, (*b*) crisscross tool marks without spindle inclination, and (*c*) unidirectional tool marks caused by negative inclination of spindle

Table 1 Advantages and disadvantages of three kinds of spindle inclination

Inclination	Positive	Zero	Negative
Advantages	(1) No back-cutting and longer tool life (2) Relatively simple and regular texture pattern	(1) Better flatness of the machined surface (2) Easier to be applied for conventional machine	(1) Relatively simple and regular texture pattern
Disadvantages	(1) Spindle tilt induced slightly concave form	(1) Back-cutting induced additional tool wear (2) Hard to control the texture pattern	(1) Severe tool wear (2) Poor surface quality

Considering workpiece geometry as well as some crucial factors of face milling mechanism, the HDM-based methodologies for addressing related problems have been further studied by scholars in recent years. Wang et al. [35] developed a framework for efficient monitoring of spatial variation in HDM data using principal curves and quality control charts. Based on the sequential strategy for global and localized monitoring of shape variations in HDM data, Suriano et al. [36] proposed an improved framework for HDM data collected from an automotive engine head machining process, resulting in good effectiveness for localizing the defective regions on the out-of-control parts. By altering the tool feed rate to match the axial force on the cutter with the local compliance of the workpiece, Tai et al. [37] proposed a feed rate optimization method for improvement of surface flatness in face milling based on HDM. Considering workpiece geometry and processing parameters, Zhou et al. [38] developed a functional morphing method by using the surface HDM data before the face milling process and the process variables to predict the surface quality afterward in multistage manufacturing. Nguyen et al. [39] proposed a physical model to monitor the spindle setup tilt and deflection using surface data measured by HDM. Over reliance on data-driven or statistical methods might show limitations when facing cases with more complex physical processes. However, according to the review of the state-of-the-art, the existing physical models are not comprehensive enough to reflect the real physical process during face milling. Furthermore, the utilization of HDM data mainly focuses on flatness, whereas the waviness information is seldom mined due to the lack of effective evaluation of the waviness characteristics (especially for tool marks). The common waviness parameters defined by the International Organization for Standardization (ISO) are hard to be connected with processing parameters through physical modeling, because ISO parameters are general evaluation indexes for various surface textures, disregarding the specific morphological features of tool marks. This research is greatly motivated by these limitations, since waviness is a major component of surface texture and thus quite important for surface quality improvement.

In summary, surface texture with tool marks has not been evaluated appropriately by using HDM data, bringing a unique challenge to physical modeling for tool marks of workpieces with discontinuous surfaces in face milling. To overcome this challenge, a novel and detailed HDM-based approach for surface texture quality improvement is proposed. First, the evaluation indexes for tool marks are defined based on HDM data preprocessing, which are proposed to replace the ISO waviness parameters for surface texture quality prediction by physical modeling. Second, the physical modeling of tool marks is presented. The effects of insert runout, tool wear, and chatter stability on surface texture generation are comprehensively considered in this physical model. Third, the physical-informed optimization model is developed, and then solved by the nondominated sorting genetic algorithm-II (NSGA-II) [40], so as to find out the optimal processing parameters for surface quality improvement. At last, in order to verify the effectiveness of the proposed approach, an experimental case study is conducted on the four-cylinder engine blocks. The major contribution of this research lies in revealing physical mapping relationship between face milling mechanism (directly depended on processing parameters and workpiece geometry) and the evaluation indexes of surface texture with tool marks, with comprehensive consideration of spindle tilt, runout, tool wear and chatter stability, which has not been effectively studied according to the literature review.

The remainder of this research is organized as follows. Section 2 exhibits the specific procedures of the proposed approach, including HDM data preprocessing, physical modeling and physics-informed optimization modeling. In Sec. 3, the effectiveness of the proposed approach is demonstrated by a case study on the face milling process of a typical workpiece with discontinuous surfaces, and the experimental results are discussed and analyzed in detail. Section 4 is devoted to the conclusion from this research.

2 The Proposed Approach

The framework of the proposed approach is shown in Fig. 3, and the main steps of this approach are demonstrated as follows.

Step 1: The raw data measured by HDM is preprocessed by outlier removal and filtering. And the tool marks can be extracted from the filtered point cloud of surface texture. In order to evaluate the characteristics of tool marks, three evaluation indexes are defined.

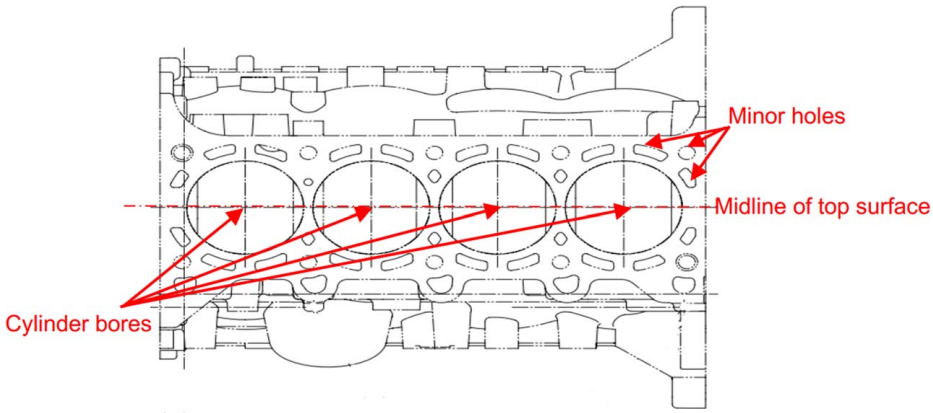

Fig. 2 Top view of a four-cylinder engine block

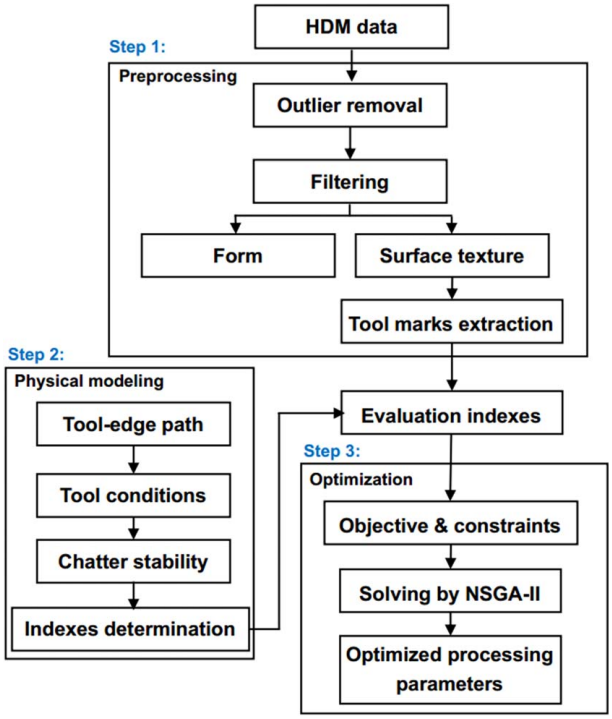

Fig. 3 Framework of the proposed approach

Step 2: Taking the face milling process of a typical workpiece with discontinuous surface as an instance, the physical model of surface texture with tool marks is developed. The tool-edge path generation is studied, which is the main component of surface texture with tool marks. Furthermore, considering the discontinuous cutter-workpiece engagement mode, the effects of tool conditions and chatter stability on surface texture are also analyzed, respectively. As a result, the evaluation indexes are determined based on the physical model.

Step 3: The physical-informed optimization model is built, aimed at quality improvement of surface texture. The variables are the common processing parameters utilized in face milling. The objective is to concurrently optimize the evaluation indexes of tool marks, so as to minimize the waviness of the face milled surface. The main constraints are cutting stability and practical operation feasibility. Since the mathematical relationships between processing parameters and the evaluation indexes are quite complex, this problem is a multi-objective and nonlinear programming. As a sophisticated algorithm for multi-objective optimization [41,42], the NSGA-II is used to solve this optimization model. And the optimized processing parameters are applied in real experiments to verify the effectiveness of the proposed approach.

2.1 HDM Data Preprocessing

2.1.1 Outlier Removal and Filtering. In practical engineering, the raw data measured by HDM may contain some redundant information such as outliers and low-pass components. Generally, the outliers can be divided into two types (see Fig. 4). Type A: the isolated and invaginated points on the measured surface, which could be induced by the ambient light interference or the reflective properties of the measured surface. Type B: the extremely protruding points, which are obviously higher than the nominal height of the surface, and usually generated by dust or carbon deposition on the measured surface. Both the two types of outliers are disadvantageous to characteristic extraction and analysis. Besides, the HDM data consists of form (low-pass) and surface texture (high-pass). Nevertheless, the form error is not the focus of this research, and the surface texture could be obtained by appropriate decomposition of HDM-based point cloud data. Therefore, outlier removal and filtering are both necessary.

For a specific workpiece, the nominal distance from the measured surface to the datum plane is known, and the difference between the measured value and the nominal height can be obtained. By setting a tolerance of the maximum difference as the threshold, the outliers could be recognized. In other words, if the Z-axis coordinate value of a data point P is larger than the threshold, the point P is regarded as an outlier. More details about threshold setting for outlier removal could refer to literature [23].

After the outlier removal, the HDM data could be decomposed into form and surface texture according to the frequency coefficients. As recommended in the ISO 16610-21 [43], the areal Gaussian filter is the current standard filtering technique for 3D surface. However, when applied to discontinuous surfaces, areal Gaussian filter might cause fatal edge distortions in the filtered results, which would reduce data accuracy. In order to eliminate the edge effect, an extended tetrolet transform method proposed by literature [25] is utilized for filtering in this research.

2.1.2 Tool Marks Extraction. In the face milling process with a multi-insert disc milling cutter, the tool-edge rotates around the centerline of the spindle, and the cutter head moves along the feed direction. Therefore, the general shape of a single tool mark is cycloidal. Taking the face milled top surface of an engine block as an instance, the cycloidal tool marks are exhibited in Fig. 5.

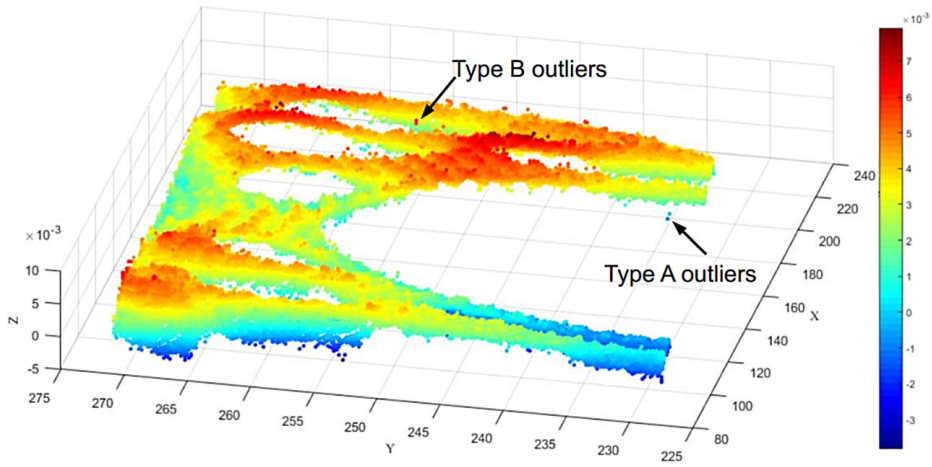

Fig. 4 Outliers in raw HDM data

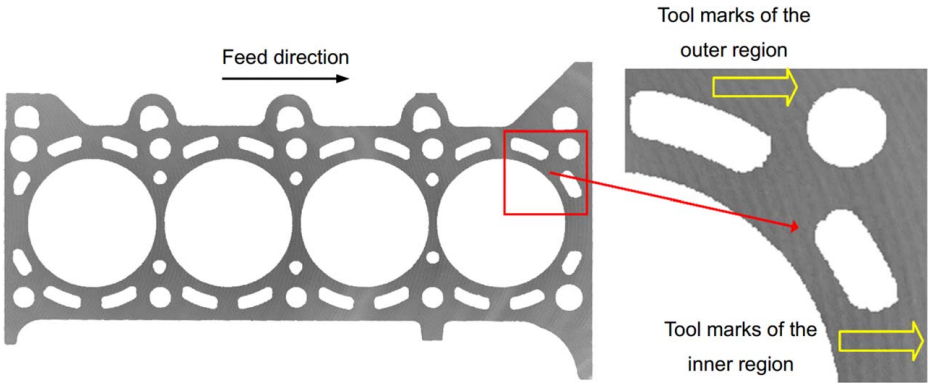

Fig. 5 Original cycloidal tool marks on the face milled top surface of an engine block

Since the direction of the tool-edge path continuously varies with processing time, the shape features of tool marks measured in different regions are inconsistent. For example, along the feed direction, the interval between two adjacent tool marks of the outer region is evidently larger than that of the inner region. In general, shape features perpendicular to the feed direction can best reflect the characteristics of the tool marks [44]. Therefore, it is necessary for tool marks extraction to transform the cycloidal tool marks into straightened ones, which are always perpendicular to the feed direction.

The straightening transformation is applied to the original cycloidal tool marks, which is suitable for the face milling cases without back-cutting. As shown in Fig. 6, arc $\widehat{AC}$ represents a cycloidal tool mark produced by the tool-edge path of a single insert within one revolution. The disc milling cutter is feeding along the X-axis at the rate of f, and the spindle speed is Ω. Denoting the radius of the disc milling cutter as R, the initial coordinates of the cutter center as $[x_O, y_O]$, and the machining time when the insert arriving at an arbitrary point B on arc $\widehat{AC}$ as t_B respectively, the coordinates of point B are given by

$$\begin{cases} x_B = x_O + R\sin\Omega t_B + f t_B \\ y_B = R\sin\Omega t_B \end{cases} \tag{1}$$

By straightening transformation, the coordinates of point B′ on the corresponding straightened tool mark can be formulated by

$$\begin{cases} x_{B'} = x_C = x_O + R + f\dfrac{\pi}{2\Omega} \\ y_{B'} = -\int_{\pi/2\Omega}^{t_B} \sqrt{\left(\dfrac{dx_B}{dt}\right)^2 + \left(\dfrac{dy_B}{dt}\right)^2}\, dt \end{cases} \tag{2}$$

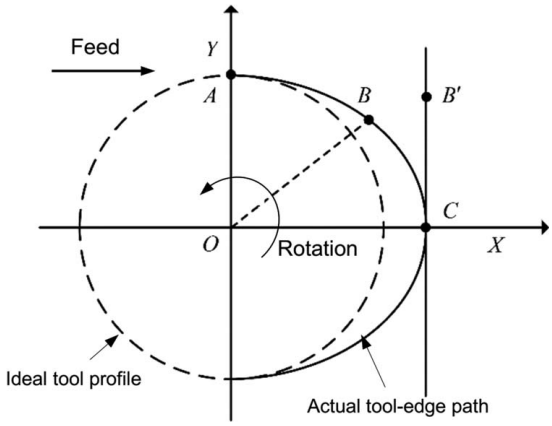

Fig. 6 Straightening transformation for face milling induced tool marks

As depicted in Fig. 7, the cycloidal tool marks have been transformed into the straightened ones. The shape features measured for tool marks of the inner region are consistent with those of the outer region, which has significantly enabled the characteristic extraction of tool marks.

2.1.3 Evaluation Indexes Definition. According to the latest ISO standard [45], a series of areal surface texture parameters have been explicitly defined and widely adopted by the industry, such as height parameters (S_q, S_p, S_v, S_z, S_a), shape parameters (S_{sk}, S_{ku}), and spatial parameters (S_{al}, S_{tr}), etc. Nevertheless, these ISO parameters are general evaluation indexes for areal surface texture, and all of them are data-driven and result-oriented. The physical relationship between indexes and machining process is hard to be clarified, which means there is a lack of linkage between the processing mechanism and surface texture, especially for tool marks induced by face milling.

In order to quantitatively describe the characteristics of the surface texture with tool marks based on the physical model proposed in this research, three types of morphological evaluation indexes are defined. As shown in Fig. 8, the evaluation indexes consist of the average peak-valley difference h_d, the wavelength spacing s_λ, and the height fluctuation h_f. The nominal peaks are marked by solid lines while the nominal valleys are marked by dotted lines. Note that even though the HDM data has been effectively cleaned up by outlier removal, filtering and tool marks extraction, the morphology of surface texture with tool marks might still not be an approximate sine wave. Instead, a concave phenomenon might occur and the lowest height of the peak of a single tool mark is termed as the concaved peak, which is marked by dashed lines in Fig. 8. The reasons could lie in two aspects. On the one hand, along the X-axis, the amplitudes of each tool mark would be different owing to tool wear and insert runout. On the other hand, along the Y-axis, the height of a single tool mark is nonconstant, which is commonly induced by spindle tilt. Different from the form error, there is no need for height fluctuation to be eliminated by filtering, because it contains the micro characteristics of surface texture and it should remain.

Considering a set of consecutive adjacent tool marks in the sampling area, numbered in sequence as $\{1, 2, \ldots, s\}$, the average peak-valley difference is defined by the mean of height differences between the nominal peak and its corresponding nominal valley for every single tool mark, and thus it can be formulated by

$$h_d = \frac{1}{s}\sum_{i=1}^{s}(\max\{z_i\} - \min\{z_i\}) \tag{3}$$

where z_i is the set of Z-axis coordinates of the data points on the ith tool mark. Basically, the average peak-valley difference h_d has the most significant impact on surface waviness, which is recommended to be kept as low as possible for surface quality improvement.

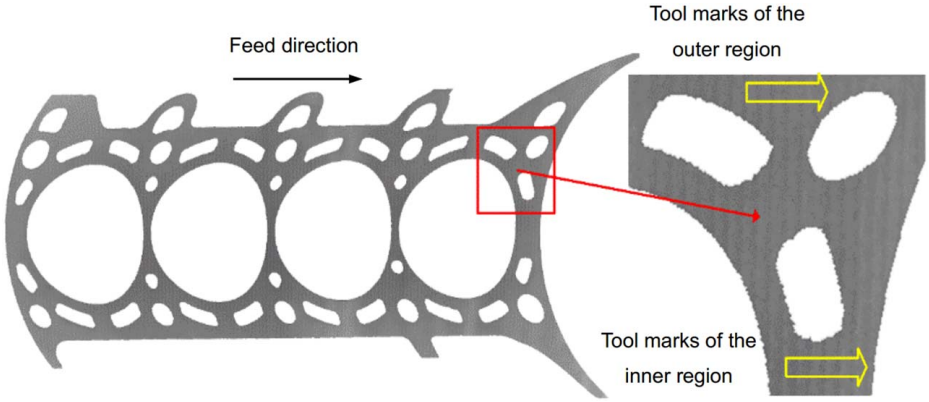

Fig. 7 Straightened tool marks on the face milled top surface of an engine block

After the straightening transformation, all the tool marks are perpendicular to the feed direction (X-axis), and the abscissas of the peaks of tool marks can be denoted by $\{x_1, x_2, \ldots, x_s\}$, respectively. Since the sampled tool marks are equidistant from each other, the wavelength spacing s_λ is a constant. To reduce the influence of measurement error, s_λ is obtained by averaging the tool mark intervals as

$$s_\lambda = \frac{1}{s-1}\sum_{i=1}^{s-1}(x_{i+1} - x_i) \tag{4}$$

The wavelength spacing s_λ greatly affects the selection of cutoff wavelength λ_f, which is utilized for distinguishing the waviness components from the form components [46]. For the accurate evaluation of waviness, the difference between s_λ and λ_f, i.e., the value of $\lambda_f - s_\lambda$, should be kept as large as possible. In this research, λ_f is set to 0.8 mm, as one of the recommended values of λ_f according to the ISO standard [47].

As for the third evaluation index h_f, it reflects the height fluctuation of a single straightened tool mark, regardless of the form error of the machined surface. For the sampled area, the height fluctuation is defined by the mean of height differences between the nominal peak and its corresponding concaved peak for every single tool mark, and thus it can be formulated by

$$h_f = \frac{1}{s}\sum_{i=1}^{s}(\max\{z_i | x = x_i\} - \min\{z_i | x = x_i\}) \tag{5}$$

where $\{z_i | x = x_i\}$ denotes the set of Z-axis coordinates of the data points on the peak of the ith tool mark. The larger h_f is, the worse the quality of surface texture will be.

2.2 Physical Modeling. The machined surface texture is directly correlated with material removal during the face milling process, and strongly influenced by multiple contributing factors such as tool conditions, dynamic characteristics, and processing parameters. Therefore, a comprehensive physical model of face milling process is needed for establishing the mapping relationship between quality evaluation indexes and the most concerned contributing factors. In this research, the physical model is established with consideration of spindle tilt, runout, tool wear, and chatter stability.

The general schematic diagram for face milling process is shown in Fig. 9. Practically, the whole face milling process often contains rough and precise operations. The material removal might also be achieved by several passes, including n_a times of axially parallel passes and n_r times of radially parallel passes. The cumulative radial cutting depth S_{ae} equals to n_r times the actual radial cutting depth a_e. Similarly, the cumulative axial cutting depth S_{ap} can be calculated by $S_{ap} = n_a a_p$.When a large disc milling cutter is utilized, only one radial pass will be enough for radial material removal, i.e., $n_r = 1$ and thus $S_{ae} = a_e$. Besides, there could be a bias from the geometric central line (GCL) of the disc milling cutter to the GCL of the workpiece, denoted by Δe, which is unfavorable for mathematical deduction. Hence, the proposed physical model is focused on a single pass of the disc milling cutter with a tool path coinciding

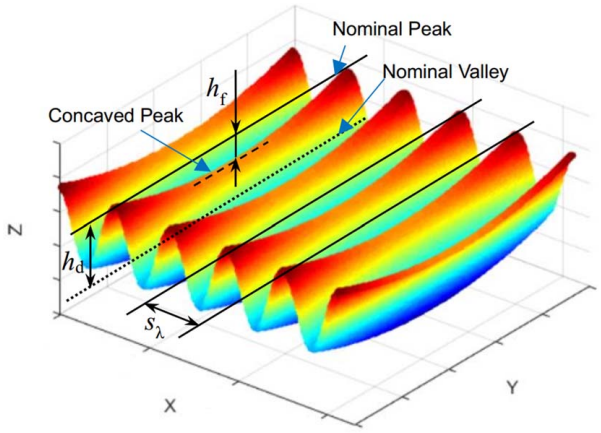

Fig. 8 Evaluation indexes for surface texture with tool marks

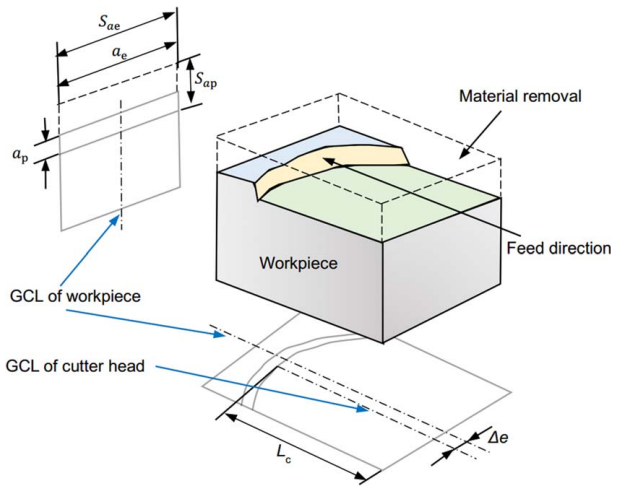

Fig. 9 General schematic diagram for face milling process

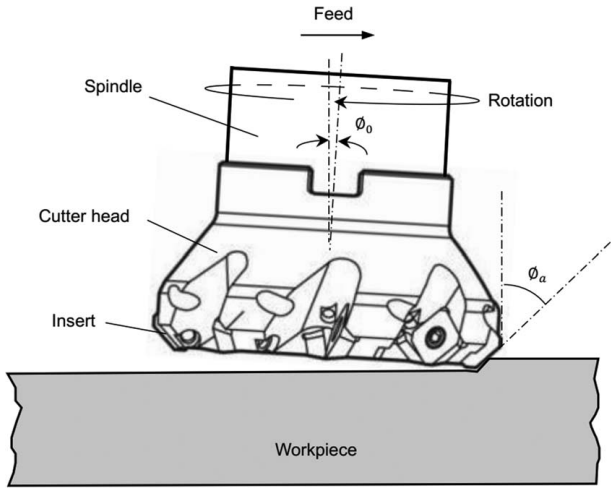

Fig. 10 Face milling with a large cutter head and a tilted spindle

with the GCL of the workpiece. In other words, n_a is set to 1 while Δe is set to 0 in this research for mathematical convenience.

2.2.1 Tool-Edge Path Generation. The tool-edge path is one of the main components of tool marks, especially for the cases utilizing a large disc milling cutter and a tilted spindle. As shown in Fig. 10, the cutter head is mounted on a spindle having a small inclination ϕ_0 in the feed direction, which makes the bottom plane of the cutter head and the workpiece surface nonparallel. The actual lead angle of the cutting insert ϕ_a is also affected by the spindle tilt.

The top view of the setup of a general face milling case is exhibited by Fig. 11. The insert-workpiece engagement point counterclockwise rotates around the center of the disc milling cutter at the speed of Ω, which is feeding along the X-axis direction at the rate of f. There are N serial numbered inserts mounted on the cutter head in total. By starting timing from the actual contact between the inserts and the workpiece, for a given cutting duration t_c, the tool-edge path generated by the first engaged insert can be formulated as

$$\begin{cases} x_1 = ft_c + R_I \cos(\theta + \Omega t_c) \\ y_1 = R_I \sin(\theta + \Omega t_c) \end{cases} \tag{6}$$

where R_I is the corrected radius of the circle formed by the contact point between tool insert and workpiece, and θ represents the angle between the feed direction and the line from the first engaged insert to the center of the cutter head.

Note that R_I is different from the radius of the cutter head R due to the spindle tilt, which can be approximately formulated as

$$R_I = \frac{1 + \cos\phi_0}{2} R \tag{7}$$

Assuming that all the inserts are evenly distributed on the circumference of the cutter head, the angle difference κ between insert i and insert $(i+1)$ (for $i = 1, 2, \ldots, N-1$) can be formulated as

$$\kappa = \frac{2\pi}{N} \tag{8}$$

According to the spatial distribution of the inserts, the tool-edge path generated by an arbitrary insert i can be obtained by

$$\begin{cases} x_i = ft_c + R_I \cos(\theta - (i-1)\kappa + \Omega t_c) \\ y_i = R_I \sin(\theta - (i-1)\kappa + \Omega t_c) \end{cases} \tag{9}$$

2.2.2 Effect of Tool Conditions. As one of the most important tool conditions, cutter runout usually occurs in many machining processes involving rotary cutting tools such as milling, honing, and grinding [48,49]. For face milling in particular, insert runout is a common phenomenon when using a disc milling cutter with multi-inserts. Without the insert runout, all the insert-workpiece engagement points can be deemed equidistant from the nominal axis of the spindle, which means all the inserts participate equally in face milling. However, once the insert runout occurs, the actual material removal process will be more complicated due to the varying radii of insert-workpiece engagement points.

In practical face milling process, inserts with wiper edges have been widely utilized to obtain machined surfaces with better flatness [50,51]. For example, a typical square insert with four symmetric wiper edges is shown in Fig. 12. The thickness of the insert is l_T, and there are four general cutting edges with a length of l_G as well as four wiper edges with a length of l_W. The intersection angle between the adjacent general cutting edge and the wiper edge is denoted by α. Assuming that the feed per insert is f_z at a constant feed rate of f, the thickness of undeformed chip is a function of the lead angle ϕ and the feed per insert f_z. Moreover, the actual lead angle of the insert mounted on the cutter head can be

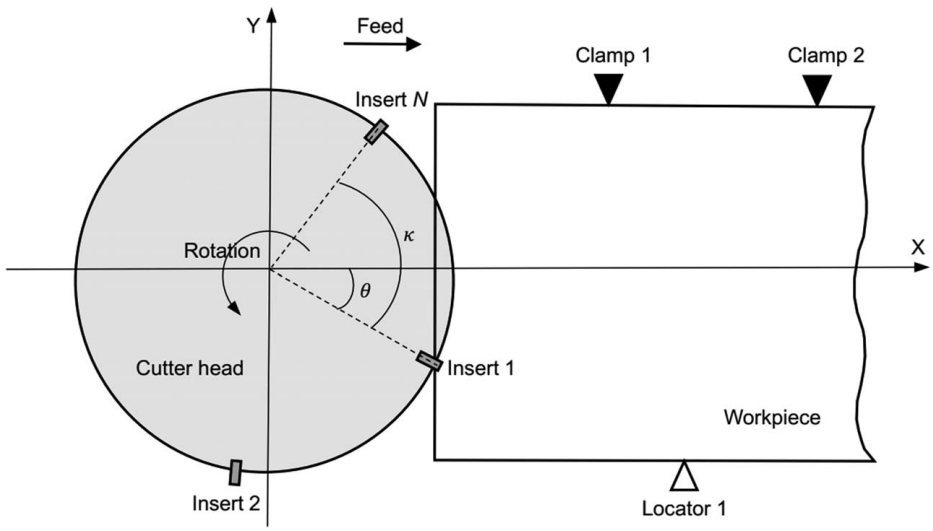

Fig. 11 Top view of a general face milling case

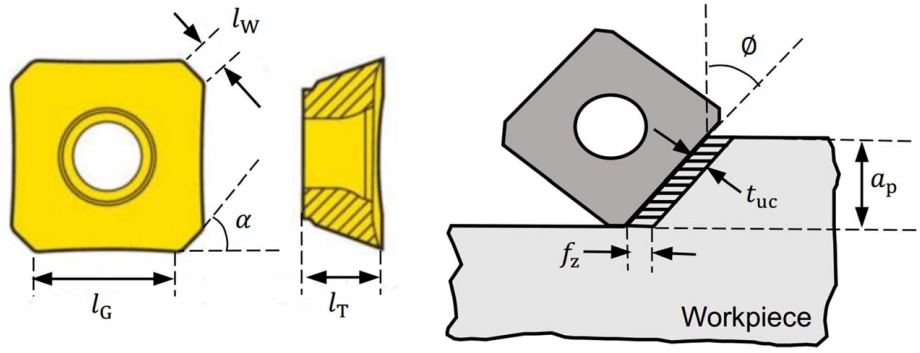

Fig. 12 The square insert with wiper edges and corresponding undeformed chip

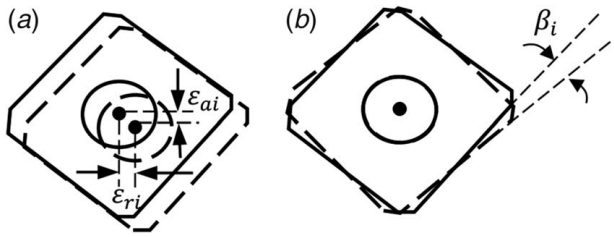

Fig. 13 Insert runout errors: (*a*) axial and radial runout errors and (*b*) rotational runout error

obtained by $\phi_a = \phi + \phi_0$ in case of the spindle is slightly tilted with an inclination of ϕ_0. Therefore, the thickness of undeformed chip can be formulated as

$$t_{uc} = f_z \cos \phi_a \tag{10}$$

As depicted in Fig. 13, the radial, axial, and rotational runouts of insert i are denoted by ε_{ri}, ε_{ai}, and β_i, respectively, for $i = 1, 2, \ldots, N$. All of these insert runouts contribute to the deviation of chip removal, leading to imperfections of the surface texture. To further investigate the effect of insert runout on surface quality, the radial and axial runouts are visualized as the state of insert-workpiece engagement points rotating around a biased axis, which is slightly different from the original spindle axis. Meanwhile, the rotational runout error of insert can be accumulated to the spindle tilt, directly affecting the actual leading angle as well as the thickness of undeformed chip. Therefore, considering the spindle tilt, the effect of insert runouts on chip removal can be expressed as

$$\begin{cases} a'_{p\_i} = a_p + \varepsilon_{ai} \\ t'_{uc\_i} = (f_z - \varepsilon_{ri}) \cos(\phi + \phi_0 + \beta_i) \end{cases} \tag{11}$$

where the subscript i is the serial number of inserts, while a'_p and t'_{uc} correspond to the actual axial cutting depth and thickness of undeformed chip, respectively.

Since the surface texture is also strongly affected by tool wear [52,53], the features of undeformed chips are studied in this research, considering two typical types of tool wear including local chipping and flank wear. As shown in Figs. 14(*a*) and 14(*b*), a general undeformed chip i is defined by the interfaces between itself and two consecutive inserts numbered by insert i and insert $i-1$ respectively. Parallel to the feed direction (X-axis), section B-B is assumed to be passed through by the GCL of the workpiece. Figure 14(*c*) exhibits section B-B of chip i and the included angle between the wiper edge and the ideal horizontal, denoted by γ_i. Besides, Fig. 14(*d*) shows the effect of tool wear on chip removal, which is responsible for the decrease of the effective cutting area for insert i.

Due to the angle between wiper edge and ideal horizontal, the actual axial cutting depth as well as the area of the section A-A is no longer constant, and evidently varies with the distance between section A-A and section B-B denoted by L. As illustrated in Fig. 15, when getting closer to the GCL of the cutter head, the actual axial cutting depth increases nonuniformly.

Denoting the intersection of chip edge trace and the GCL of cutter head along feed direction by B_0, as for an arbitrary reference point A_0 on the trace, the variation of the axial cutting depth is derived as

$$\Delta a_p(L_0) = \left(R_I - \sqrt{R_I^2 - L_0^2}\right) \tan \gamma_i \tag{12}$$

where L_0 is the projection distance from A_0 to the GCL of cutter head, ranging from 0 to $a_e/2$.

Consequently, the actual axial cutting depth of A_0 can be given by

$$a_p(L_0) = a'_{p\_i} - \left(R_I - \sqrt{R_I^2 - L_0^2}\right) \tan \gamma_i \tag{13}$$

where γ_i is jointly determined by spindle tilt, rotational insert runout, and insert geometry, formulated as $\gamma_i = \phi_0 + \beta_i + \alpha + \phi - \pi/2$.

To obtain the quantitative description of the effect of tool wear on chip removal, the geometry features of the effective cutting area for insert i are studied considering typical tool wear (see Fig. 16). By establishing a local coordinate system in section B-B of chip i, the maximum height wear of the wiper edge can be defined by

$$H_i = \max\{z_{i,b_i}\} \tag{14}$$

where the subscript $b_i = 1, 2, \ldots, B_i$ is the serial number of local chipping on the wiper edge of insert i, and z_{i,b_i} is the corresponding ordinate value (Z-axis) with respect to the local coordinate system.

Furthermore, the general height wear of the wiper edge h_i is a concern as well, since it provokes a direct decrease in the axial cutting depth. The steps to obtain h_i can be found in Appendix A.

2.2.3 Effect of Chatter Stability. Once the chatter occurs during the face milling process, the tool marks will be abnormally obvious, and the corresponding surface texture quality will be tremendously damaged and thus unacceptable. Therefore, chatter stability is needed to be considered to avoid the appearance of chatter as far as possible. Chatter stability can be studied based on the dynamics model of the cutter-workpiece system. As a widely adopted assumption for chatter related studies [54–56], the face milling system can be simplified to a two-degree-of-freedom (2-DOF) vibration system for the convenience of dynamics modeling.

The chatter stability is dependent on the dynamic response of the vibration system, which is commonly expressed by the frequency response function (FRF). For the 2-DOF vibration system, the

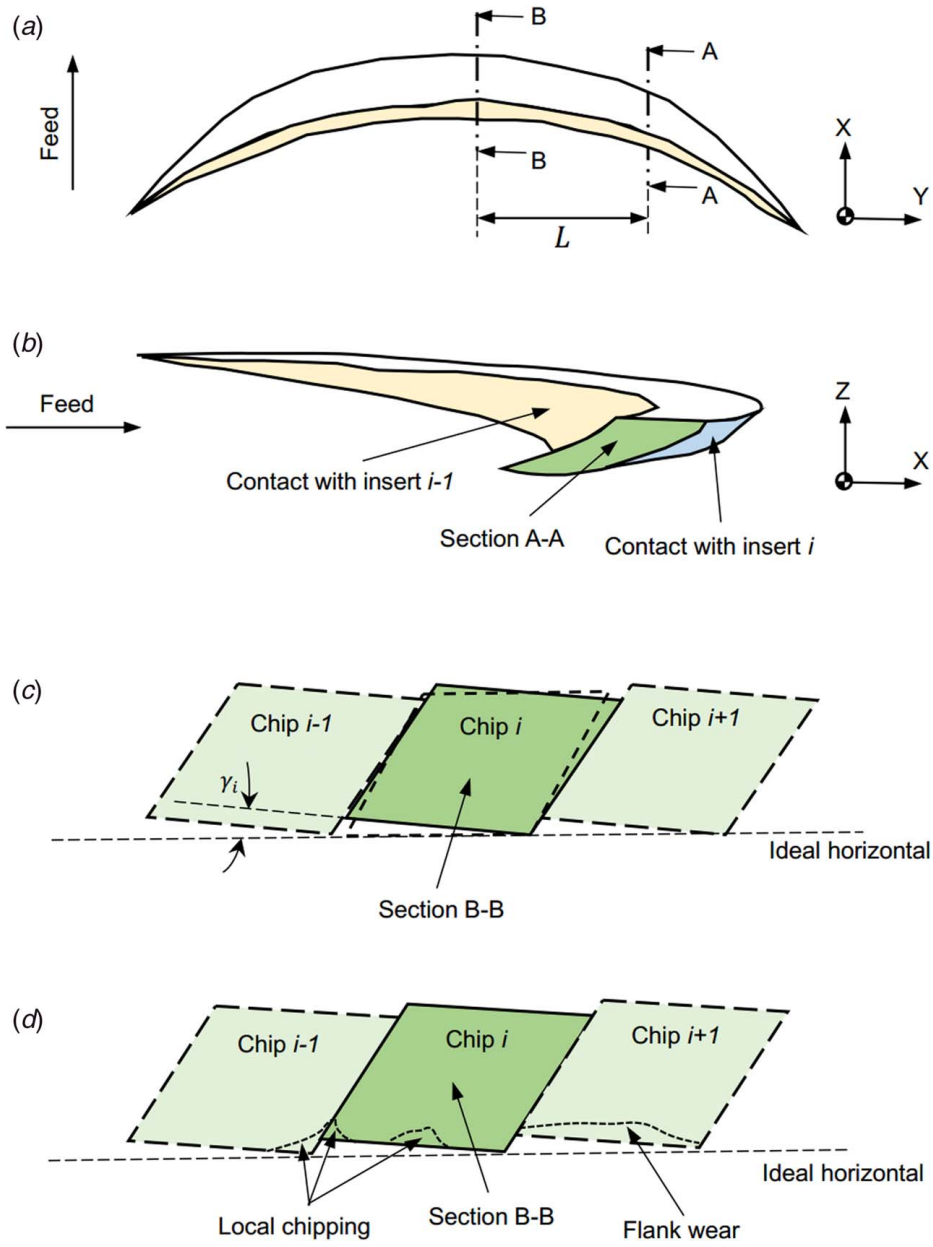

Fig. 14 The undeformed chip considering spindle tilt: (*a*) top view of chip *i*, (*b*) section A-A of chip *i*, (*c*) section B-B of chip *i* without tool wear, and (*d*) section B-B of chip *i* with different types of tool wear

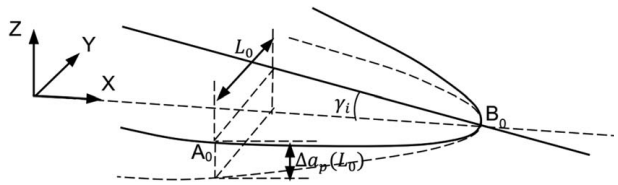

Fig. 15 Variation of axial cutting depth induced by the angle between wiper edge and ideal horizontal

FRF at the chatter frequency ω_c can be expressed in the matrix form as

$$[G(\mathrm{i}\omega_c)] = \begin{bmatrix} G_{xx}(\mathrm{i}\omega_c) & G_{xy}(\mathrm{i}\omega_c) \\ G_{yx}(\mathrm{i}\omega_c) & G_{yy}(\mathrm{i}\omega_c) \end{bmatrix} \tag{15}$$

where i denotes the unit of imaginary number. Note that the chatter frequencies could be multi-order and distributed in principle around the dominant modes of the vibration system, which could be obtained by simulations or vibration tests.

Taking the regenerative effect into consideration, at an arbitrary moment t during the machining process, the regeneration displacement vector is denoted by $\{\Delta(t)\}$. Given the directional coefficient matrix $\boldsymbol{\alpha}$ as a time-independent function of the radial immersion angle of the milling cutter, the dynamic cutting force model for the face milling process can be formulated as

$$\{F(t)\} = \frac{N_e a_p}{4\pi} K_t \boldsymbol{\alpha} \{\Delta(t)\} \tag{16}$$

where N_e is the number of inserts engaged with the workpiece, while K_t is the tangential cutting coefficient of the exponential instantaneous cutting force model [57].

However, the accuracy of the dynamics model is directly affected by the radial cutting depth a_e as well as the axial cutting depth a_p. For workpieces with discontinuous surfaces in particular, the actual radial cutting depth varies with the cutting distance L_c, which is

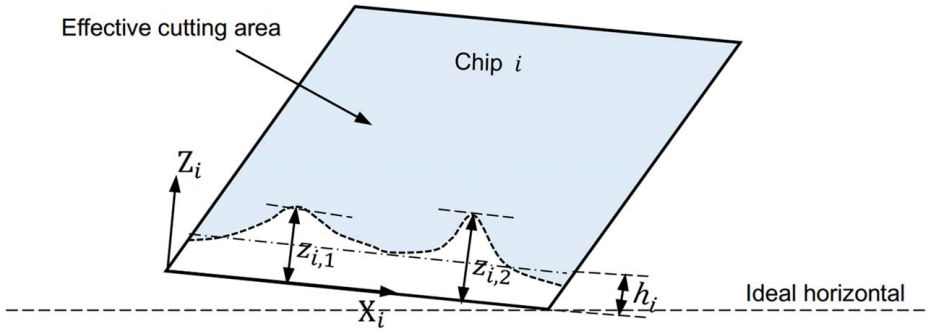

Fig. 16 Effective cutting area for insert *i* considering typical tool wear

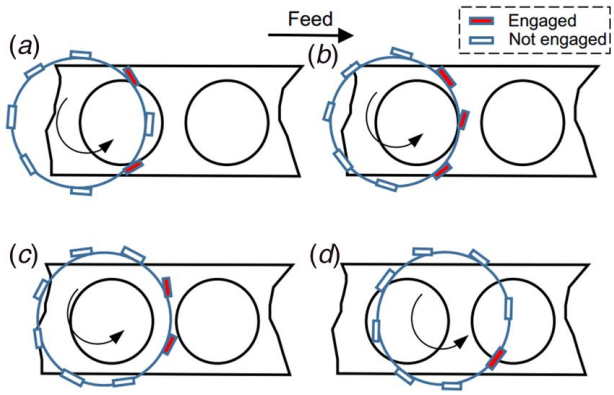

Fig. 17 Variation of cutting insert engagement: (*a*) $N_e = 2$, (*b*) N_e switches from 2 to 3, (c) N_e switches from 3 to 2, and (*d*) N_e switches from 2 to 1

determined by the cutting duration t_c and the feed rate f. Besides, the actual axial cutting depth also keeps changing during the face milling process, due to the effects of spindle tilt, insert runout, and tool wear as previously mentioned.

As illustrated in Fig. 17, the top surface of a typical workpiece with multiple cylinder bores is milled by a large disc milling cutter. The number of inserts engaged with the workpiece N_e varies as the cutter feeding. The face milling process is intermittent due to the discontinuity of the machined surface, and there is a step decrease of N_e as the cutter reaching the cylinder bores, and vice versa. Since $\{F(t)\}$ is a function of N_e, according to Eq. (16), the variation of N_e cannot be neglected in favor of the modeling accuracy. Based on the previous work proposed by the authors [58], the variation pattern of N_e is complex yet computable for general cases, which can be formulated by

$$N_e = \left\lceil \frac{NC_a(t)}{2\pi R} \right\rceil \tag{17}$$

where $C_a(t)$ is the total length of the cutting arcs at an arbitrary moment t within the range of $[0, t_c]$, and the mathematical operator $\lceil\rceil$ means rounding up the filled value.

By properly calculating the time-dependent total cutting arc length with consideration of workpiece geometry, the dynamics model of the face milling process can be corrected by Eq. (17). As a result, the critical value of the axial cutting depth and its corresponding spindle speed can be obtained by

$$\begin{cases} a_{p\_lim} = \dfrac{2\pi(\Lambda_R^2 + \Lambda_I^2)}{N_e K_t \Lambda_R} \\ \Omega_{lim} = \dfrac{60}{N_e((2k_L + 1)\pi - 2\arctan(\Lambda_I/\Lambda_R))} \end{cases} \tag{18}$$

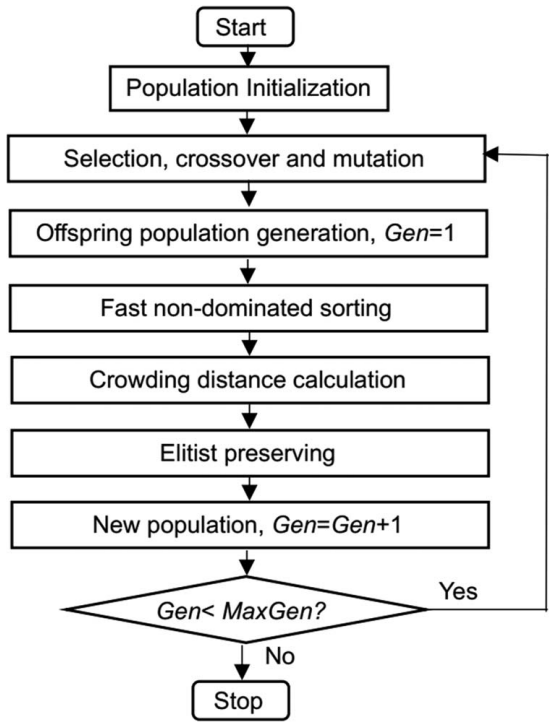

Fig. 18 Flowchart of NSGA-II utilized for optimization solution

where $k_L = 0, 1, 2\ldots$, indicating the successive stability lobes, while Λ_R and Λ_I denote the real part and imaginary part of the eigenvalue for the characteristic equation of regenerative chatter [58], respectively.

The detailed derivation for Λ_R and Λ_I can be found in Appendix B. Based on Eq. (18), the stability lobe diagram (SLD) [59] of face milling process considering workpiece geometry can be generated by iterative calculation through programming, ensuring chatter-free cutting.

2.2.4 Evaluation Indexes Determination. Since each insert mounted on the cutter head repeatedly participates in material removal at the same time interval, the effects of the tool conditions on surface texture as well as the corresponding evaluation indexes are periodic. By comprehensively considering spindle tilt, insert geometry, insert runouts, and general height wear of wiper inserts, the average peak-valley difference h_d can be determined based on the physical model of face milling and formulated by

$$h_d = \frac{\sum_{i=1}^{N} [t'_{uc\_i} \sin\gamma_i / \sin\alpha + h_i \cos(\phi + \phi_0 + \beta_i)/\cos\alpha]}{N} \tag{19}$$

Note that the actual thickness of undeformed chip t'_{uc_i} is a function of ε_{ri} according to Eq. (11), thus the effect of insert runouts on h_d is not only contributed by the rotational insert runout but also by the radial one. According to Eq. (19), since the intersection angle between general cutting edge and wiper edge (denoted by α) is fixed once the geometry of inserts is determined, for each insert, the peak-valley difference h_d is positively correlated with γ_i, h_i, and t'_{uc_i}. Meanwhile, h_d is negatively correlated with the sum of ϕ, ϕ_0, and β_i.

The wavelength spacing s_λ is mainly affected by the spindle tilt and rotational insert runout, leading to a slight deviation from the feed per insert. And it can be obtained by

$$s_\lambda = \frac{60f\sum_{i=1}^{N}\cos(\phi_0+\beta_i)}{\Omega N^2} \tag{20}$$

Equation (20) intuitively exhibits the dependency of s_λ on different processing parameters. Considering the spindle tilt condition and the rotational runout of each insert as constant during face milling process, s_λ can be easily predicted and controlled by adjusting feed rate f, spindle speed Ω, and the total number of inserts N before machining.

According to Eq. (12), the height fluctuation h_f is primarily induced by the variation of actual axial cutting depth. Taking the effect of insert runout into account, yields

$$h_f = \frac{R[1+\cos(\phi_0+\beta_i)]}{2N}\sum_{i=1}^{N}\left\{1-\sqrt{1-\frac{a_e^2}{R^2[1+\cos(\phi_0+\beta_i)]^2}}\right\} \times \tan\gamma_i \tag{21}$$

where the radial cutting depth a_e could be a variable, which depends on the cutting path, the cutter geometry, and the discontinuity of the machined surface.

The dependency of h_f on different processing parameters shows remarkable nonlinearity, which means it is hard to control it by monotonically increasing or decreasing a certain processing parameter, except for γ_i, which significantly positively correlated with the spindle tilt ϕ_0. In order to obtain an optimal machined surface, a good balance between different evaluation indexes is quite crucial.

2.3 Physics-Informed Optimization Modeling. In this research, the processing parameters to be optimized (including N, Φ_0, a_p, f, and Ω) are deemed as variable and controllable in a suitable range, which is limited by the actual engineering conditions such as the load capacity of machine tools. Meanwhile, the other contributing factors (such as spindle stiffness and workpiece material properties, etc.) are deemed as fixed or dependent on the processing parameters.

2.3.1 Objective Function. The ultimate goal of this research is to improve the quality of surface texture, which could be reflected by the proposed evaluation indexes as well as the ISO evaluation parameters. Since there is a lack of explicit expression for the relationship between ISO evaluation parameters and the processing parameters, the objective function consisting of h_d, s_λ, and h_f is more favorable to the physics-informed optimization model, taking the advantages of explicit expressions with processing parameters established by physical modeling (i.e., Eqs. (19)–(21)). In case of the weight assignment is sufficiently reasonable (primarily relying on expert experience or specific technological requirements), the multi-objective optimization problem can be transformed into the single-objective optimization, and the objective function could be defined by

$$\min W = w_1 h_d + w_2\frac{s_\lambda}{\lambda_f - s_\lambda} + w_3 h_f \tag{22}$$

where w_1, w_2, and w_3 are the corresponding weights and $w_1+w_2+w_3=1$.

In most cases, however, it is hard to properly assign the weights for each objective, and sometimes the physical meanings of each objective are completely different even after the nondimensional processing [60,61]. Moreover, both h_d and h_f significantly affect the quality of surface texture referring to the ISO parameters and thus become important, whereas s_λ mainly contributes to the selection of cutoff wavelength λ_f for waviness filtering rather than the quality of surface texture and thus becomes relatively less important. There is no need to deliberately pursue the minimum value of $s_\lambda/(\lambda_f - s_\lambda)$. That is, even if the weights for each objective could be determined, w_2 will be much less than w_1 and w_3. Therefore, in this research, the objective function is recommended to be expressed as bi-objective form and given by

$$\min W = [h_d, h_f] \tag{23}$$

Note that $s_\lambda/(\lambda_f - s_\lambda)$ is regarded as a supplementary objective, and it is deemed as acceptable for general cases when its value is less than 0.5.

2.3.2 Constraints. Due to the convenience for automatically controlling or manually changing, the variables of this physics-informed optimization model basically consist of common processing parameters, including spindle speed Ω, feed rate f, axial cutting depth a_p, spindle inclination ϕ_0, and the total number of inserts N. Hence, the optimization model is subjected to the following constraints.

Constraint 1: It is necessary for spindle speed selection to consider the material properties of the workpiece and the load capacity of the machine tool. Denoting the lower bound and upper bound of the spindle speed by Ω_{st} and Ω_{fi}, respectively, yields

$$\Omega_{st} < \Omega < \Omega_{fi} \tag{24}$$

Constraint 2: In order to ensure the cutting stability of the face milling process, a_p should be less than the critical axial cutting depth $a_{p\_lim}(\Omega)$, which can be formulated by

$$0 < a_p < a_{p\_lim}(\Omega) \tag{25}$$

Constraint 3: If the feed rate is set to an excessively small value, the machining efficiency, usually indicated by material removal rate, will be unacceptable for long term and mass manufacturing. Besides, the machine feeding accuracy also limits the lower bound f_{st} for feed rate selection. Similar to Constraint 1, the maximum feed rate f_{fi} is bounded by the load capacity of the machine. Hence, the constraint for f is given by

$$f_{st} < f < f_{fi} \tag{26}$$

Constraint 4: To improve the symmetry of the cutting forces, the total number of inserts N is commonly set to an even number in practical engineering, which has significantly reduced the feasible domain of this problem. Denoting the maximum number of inserts that can be mounted on the disc milling cutter by N^*, yields

$$N \in \{2, 4, \ldots, N^*\} \tag{27}$$

2.3.3 Optimization Solution. As one of the most popular multi-objective search-based algorithms, NSGA-II has the advantages of good convergence of solution set and fast computing speed, becoming the benchmark of other multi-objective optimization algorithms [42]. Therefore, NSGA-II is used to solve the proposed bi-objective optimization model. The flowchart of NSGA-II utilized for optimization solution is illustrated by Fig. 18. Therein, *Gen* and *MaxGen* denote the number of the current generation and the maximum number of generations, respectively.

Main solution procedures based on NSGA-II include fast nondominated sorting, crowding distance calculation, and elitist preserving, which have been clearly defined by published works [40]. The other key points for the implementation of NSGA-II are given as follows.

Variable discretization: Since all the considered processing parameters except N are continuous variables, a suitable step size for each continuous variable is necessary for variable discretization. Taking engineering applicability and computing efficiency into consideration, the step sizes for Φ_0, a_p, f, and Ω are set to 0.02 deg, 0.01 mm, 10 mm/min, and 50 rpm, respectively.

Stopping criteria: The maximum number of generations is set to 1000 as the stopping criteria for the solution process in this research. In other words, once the cyclic instruction has been executed 1000 times, the NSGA-II is deemed to converge to the Pareto optimal solution set.

Pareto compromise: Since having too many Pareto optimal solutions (presented by the Pareto front) is not effective for guiding practical engineering, the population of each generation is set to 100, limiting the total number of Pareto optimal solutions. The finally selected solutions would be better to reach a compromise to avoid any objective getting too close to the extreme, i.e., solutions located on the middle part of Pareto front are preferred except for special circumstances.

3 Case Study

3.1 Experimental Setup

3.1.1 Tool Conditions Measurement. Inserts of type SEEX1204ZZTN-M14 MK1500 are utilized in this case study. In order to obtain the tool wear condition, which could affect the surface finish quality, the wiper edges of a group of randomly selected inserts are measured by optical microscope before the face milling experiments (see Fig. 19(*a*)). Limited by the measurement resolution, the accurate height wear of the wiper edge is hard to be obtained only based on the measurement results offered by the optical microscope. Therefore, the morphology of the utilized inserts is further analyzed by the field emission scanning electron microscopy (FE-SEM, Carl Zeiss Ultra 55, Germany) at 5 kV (see Fig. 19(*b*)). Meanwhile, after the inserts are mounted on the disc cutter head, the insert runouts are manually measured by a micron outside micrometer.

3.1.2 Face Milling Experiments. In this case, the four-cylinder engine blocks of type B-12 (see Fig. 20) are used to validate the

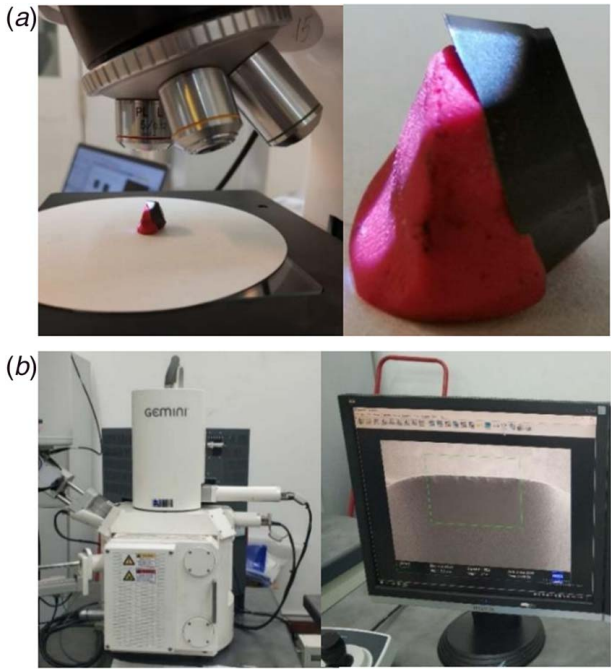

Fig. 19 Experimental setup for tool wear measurement: (*a*) the optical microscope and (*b*) the FE-SEM system

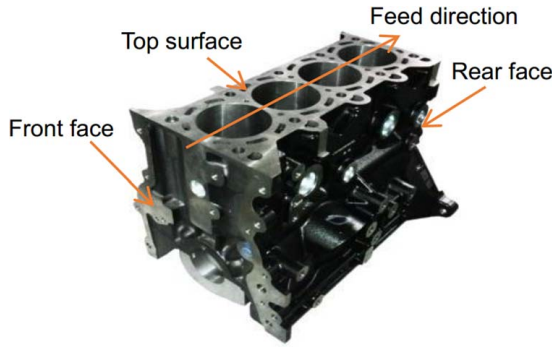

Fig. 20 Four-cylinder engine blocks utilized in face milling experiments

effectiveness of the proposed approach. As an important joint surface for assembling, the top surface of engine block is finished by face milling process with one pass of a disc milling cutter. The texture quality of the top surface is vital for sealing performance and reliability of the engine. Since the engine block is made of gray cast iron HT250, the surface hardening induced by the cutting temperatures could be effectively avoided during chip removal [62,63]. Otherwise, the appearance of surface hardening would further increase the complexity for explaining the imperfections of surface texture, which is mainly focused on by this research.

Considering the characteristics of the workpiece geometry and the machining system dynamics, the SLD for the face milling process is obtained as shown in Fig. 21. The searching range for axial cutting depth is from 0.02 mm to 0.5 mm, for feed rate from 30 mm/min to 800 mm/min, for spindle speed from 200 rpm to 2500 rpm, and for spindle inclination from 0.02 deg to 0.3 deg. By solving the proposed optimization model with NSGA-II, the Pareto optimal solution set is illustrated by Fig. 22.

According to the Pareto optimal solution set given by NSGA-II as well as the SLD of the face milling system, four sets of face milling experiments with different processing parameters are implemented on engine blocks. The detailed processing parameters for each case are given by Table 2. Therein, case (1) utilizes the original processing parameter design for practical manufacturing, which is basically depending on engineering experience. Both case (2) and case (3) are selected from the Pareto optimal solution set. Meanwhile, case (4) utilizes the recommended processing parameter design obtained by literature [13], which is selected as the benchmark for advantage validation of the proposed approach,

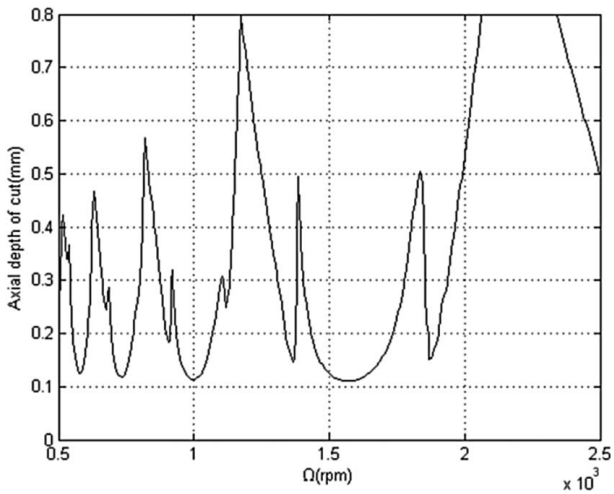

Fig. 21 SLD of the face milling system

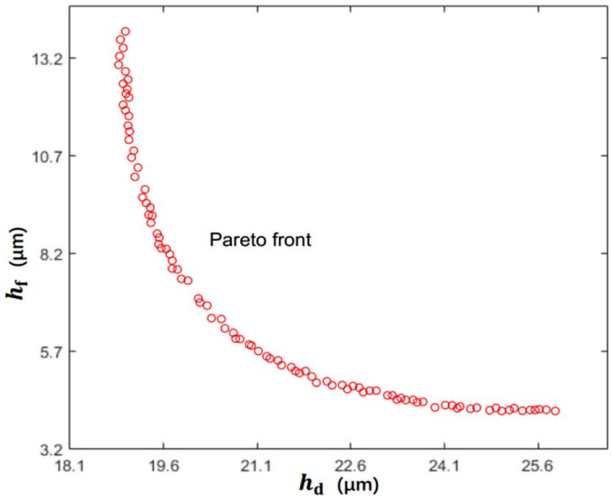

Fig. 22 Pareto optimal solution set given by NSGA-II

Table 2 Processing parameter design for face milling experiments

Case no.	f (mm/min)	a_p (mm)	Ω (rpm)	N	Φ_0 (deg)
(1)	360	0.05	950	6	0.14
(2)	400	0.1	1350	8	0.1
(3)	630	0.12	1200	8	0.2
(4)	520	0.08	1100	8	0.25

considering the relevance and reproducibility of methodology. Face milling experiments are conducted on engine blocks within the DMG-HSC-75 CNC machining center (see Fig. 23(*a*)), using a disc milling cutter with a diameter of 160 mm and a maximum capacity of 10 cubic boron nitride (CBN) inserts (see Fig. 23(*b*)).

3.1.3 Surface Finish Measurement With High Definition Metrology. To obtain the surface texture of the face milled surfaces, the 3D point cloud data of the surface finish is measured by the HDM instrument of type ShaPix3D® 3000 series. The measurement setup is demonstrated in Fig. 24.

3.2 Experimental Results and Analysis. The measurement results of tool wear by the optical microscope are shown in Fig. 25. According to the observed wear condition, inserts can be divided into two groups, i.e., the brand-new ones and the worn ones. Therein, the brand-new inserts can be set as the benchmark for height wear calculation, while typical worn inserts can be selected to be utilized in the following face milling experiments. Since the face milling experiments are conducted under laboratory conditions in a relatively short term, the newly generated wear of inserts is quite slight and thus negligible.

It can be seen from these micrographs that the coating for brand-new inserts is intact (see Fig. 25(*b*)), whereas the coating of worn inserts is seriously damaged (see Fig. 25(*c*)), which has clearly reflected the flank wear situation of the wiper edges.

Furthermore, in order to quantitatively investigate the tool wear condition, especially for the general height wear h_i, the FE-SEM system is utilized and the results are shown in Fig. 26. The local chipping on the wiper edges can be easily observed, while h_i can be calculated by comparison between the measured height and the nominal height of the wiper edge.

The measurement results of h_i are given by Table 3. There are two possible reasons for the irregular variation of h_i among different inserts. First, all of these eight inserts are randomly selected from the typical worn inserts, which are preliminarily identified by the optical microscope. Hence, the serial of h_i given by Table 3 keeps in neither ascending nor descending order. Second, since the specific service time of each insert could be different, the wear condition (reflected by h_i) of each insert might also be various.

After face milling experiments, the partial view of the top surface of one engine block is shown in Fig. 27. Visible tool marks on the machined surfaces indicate that the proposed evaluation indexes and the corresponding optimization approach are suitable for this experimental case.

As exhibited in Fig. 28, the HDM measured point cloud data is transformed into two-dimensional image form for better overall observation. Since the diameter of the disc milling cutter (160 mm) is slightly less than the maximum width of the machined top surface (171 mm), the evaluation of surface texture will be severely disturbed when facing local regions near both ends of the cutting path. Therefore, surface texture of the relatively middle region with an average width of 109 mm is selected for the study, defined by the cutting distance as 75 mm $< L_c <$ 275 mm. The selected region is entirely machined by the disc milling cutter, and it contains the geometric features of two complete cylinder bores in the middle of the cutting pass, which is sufficient for representation for the workpiece geometry characteristics.

An intuitive cognition given by Fig. 28 is that the quality of machined surfaces has been significantly improved by either the proposed model or the benchmark model. Note that the height variation amplitude of the machined surface in case (4) (see Fig. 28(*d*)) is significantly small than that of case (1) (see Fig. 28(*a*)), even though a typical central concave phenomenon is observed in case (4), indicating a better h_d yet worse h_f after optimization by the

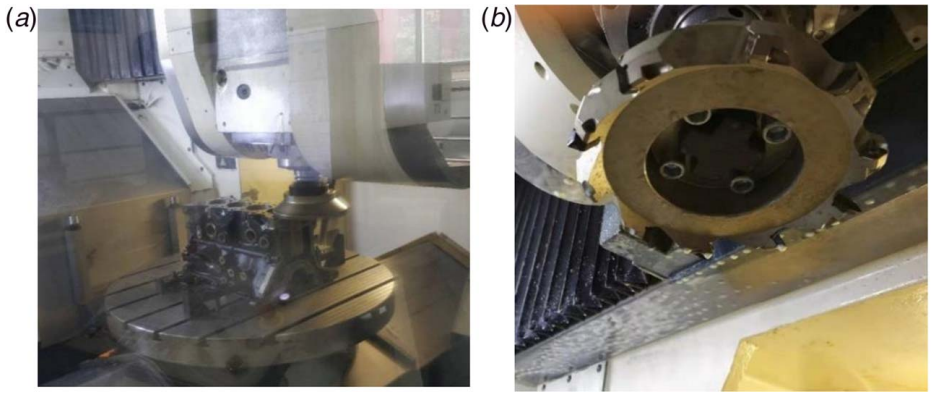

Fig. 23 Experimental setup for face milling: (*a*) fixturing in the CNC machining center and (*b*) the disc milling cutter utilized in experiments

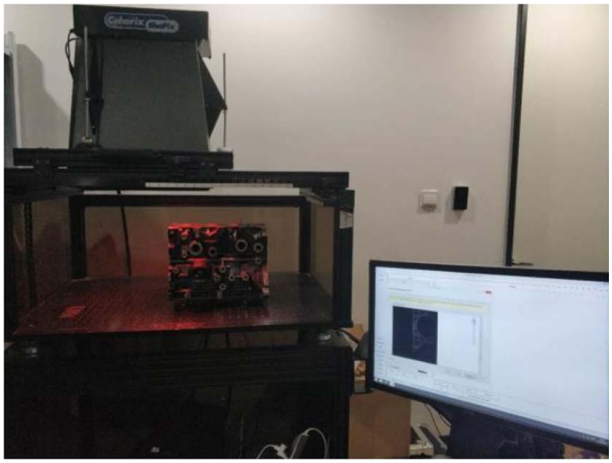

Fig. 24 Experimental setup for surface finish measurement with the HDM system

benchmark model. The possible reason for the worsen h_f is analyzed as follows. According to Eq. (12), the variation amplitude of the actual axial cutting depth is positively correlated with γ_i in a certain range. If other parameters including α, β_i, ϕ, and L_0 keep fixed, the larger ϕ_0 will lead to a larger $\Delta a_p(L_0)$, and consequently the height fluctuation of a single tool mark generated by insert i will be greater, resulting in worse h_f.

For further comparison between the effectiveness of the proposed model and the benchmark model, the characteristics of tool marks containing waviness information are needed to be mined from HDM data. Through HDM data preprocessing as introduced by Sec. 2.1, the measured evaluation indexes can be obtained for each case. Meanwhile, since all the processing parameters are known, the evaluation indexes can also be theoretically calculated based on the physical model proposed by Sec. 2.2. The comparison results are given by Table 4. Besides, the ISO areal surface texture parameters are also calculated to evaluate the surface texture quality from another perspective, which is given by Table 5.

According to these two tables, several valuable insights are obtained. First, the prediction errors of all the evaluation indexes are almost within 15%, which is deemed acceptable for practical engineering. Note that the prediction errors of case (4) do not refer to the prediction accuracy of the benchmark model, but refer to the proposed model instead. Because the utilized predictors are originally proposed by this research and the prediction values are obtained based on the proposed physical model. The possible reasons for the prediction errors consist of two aspects. On one hand, the HDM measurement conditions and senor noises might contribute to the prediction errors in a certain degree, which could be significantly controlled within an acceptable range through reasonable maintenance and standard utilization of the HDM equipment. On the other hand, even though the proposed model has tried to descript the actual physical situation as real as possible by comprehensively considering the effects of multiple inner factors, the gap between the theoretical model and the real physical process still exists, which could be further narrowed in future works.

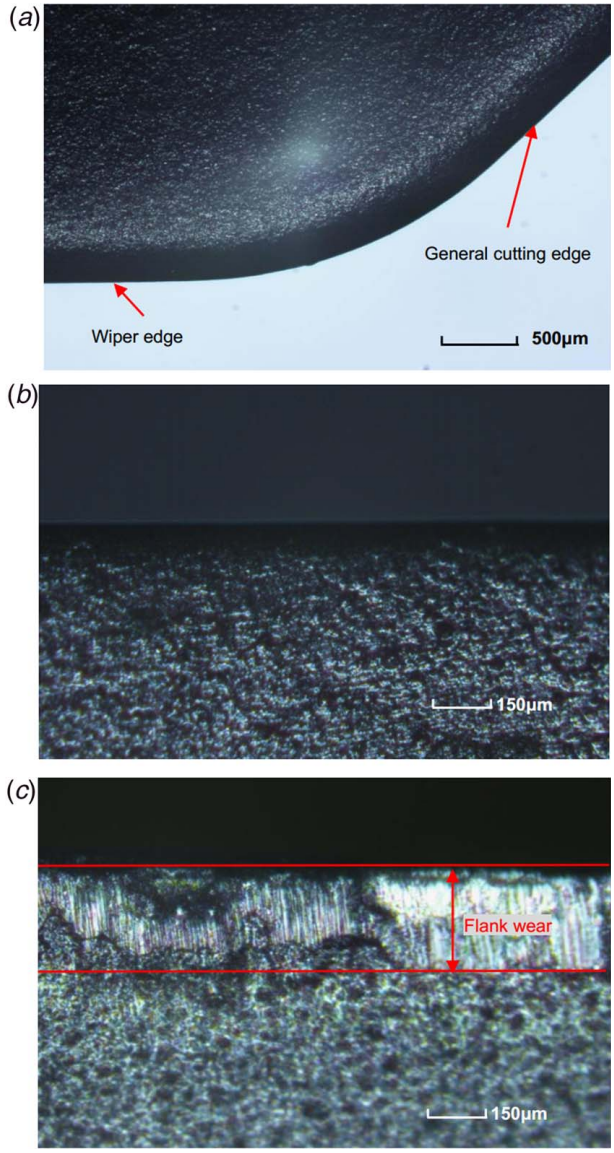

Fig. 25 Tool wear measured by the optical microscope: (*a*) overview of the insert corner, (*b*) micrograph of a brand-new wiper edge, and (c) micrograph of a worn wiper edge

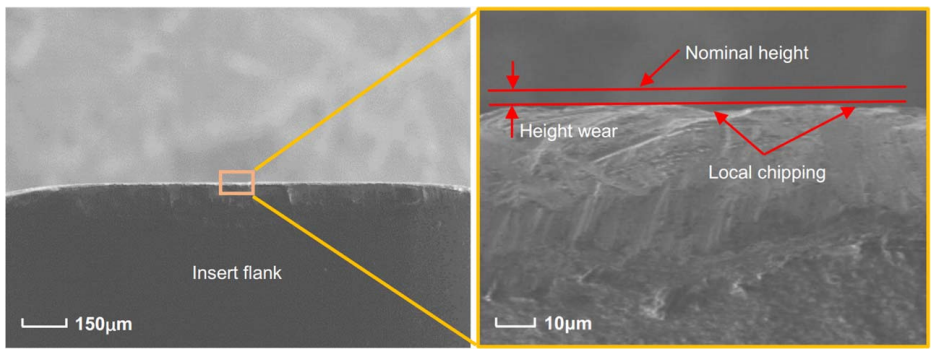

Fig. 26 Tool wear measured by the FE-SEM system

Table 3 Measurement results of general height wear of the wiper edges

Insert no.	1	2	3	4	5	6	7	8
h_i (μm)	2.3	4.2	0.2	0.8	3.3	7.5	5.3	3.6

Second, with comprehensive comparison both in the proposed evaluation indexes and the ISO parameters, the measurement results indicate that the proposed model shows better performance in surface texture quality improvement than the benchmark model. This advantage is mainly contributed by the comprehensive consideration of the effects of spindle tilt, runout, tool wear, and chatter stability. In the benchmark model, however, only the effect of spindle tilt on surface texture structuring is concerned. Since the wavelength spacing s_λ of each case meets the condition that $s_\lambda/(\lambda_f - s_\lambda)$ is less than 0.5, all cases are deemed acceptable in the aspect of s_λ. Therefore, the effectiveness of the proposed approach is further validated.

Third, since the processing parameter designs of case (2) and case (3) are chosen for the Pareto front given by NSGA-II, these two designs have their own advantages. For instance, by using a larger spindle inclination, the average peak-valley difference h_d is successfully reduced in case (3). However, the height fluctuation h_f of case (2) is evidently less than that of case (3). The experimental results indicate that h_f tents to become worse after utilizing larger spindle inclination ϕ_0, which could significantly aggravate the variation of the actual axial cutting depth during each revolution of a single insert. However, by appropriately enlarging ϕ_0, the average peak-valley difference h_d might get a better result according to Eq. (19). This insight is consistent with the proposed guideline of Pareto compromise. A good balance is necessary for practical engineering when utilizing the proposed approach.

Fig. 27 Partial view of the top surface of engine block after face milling

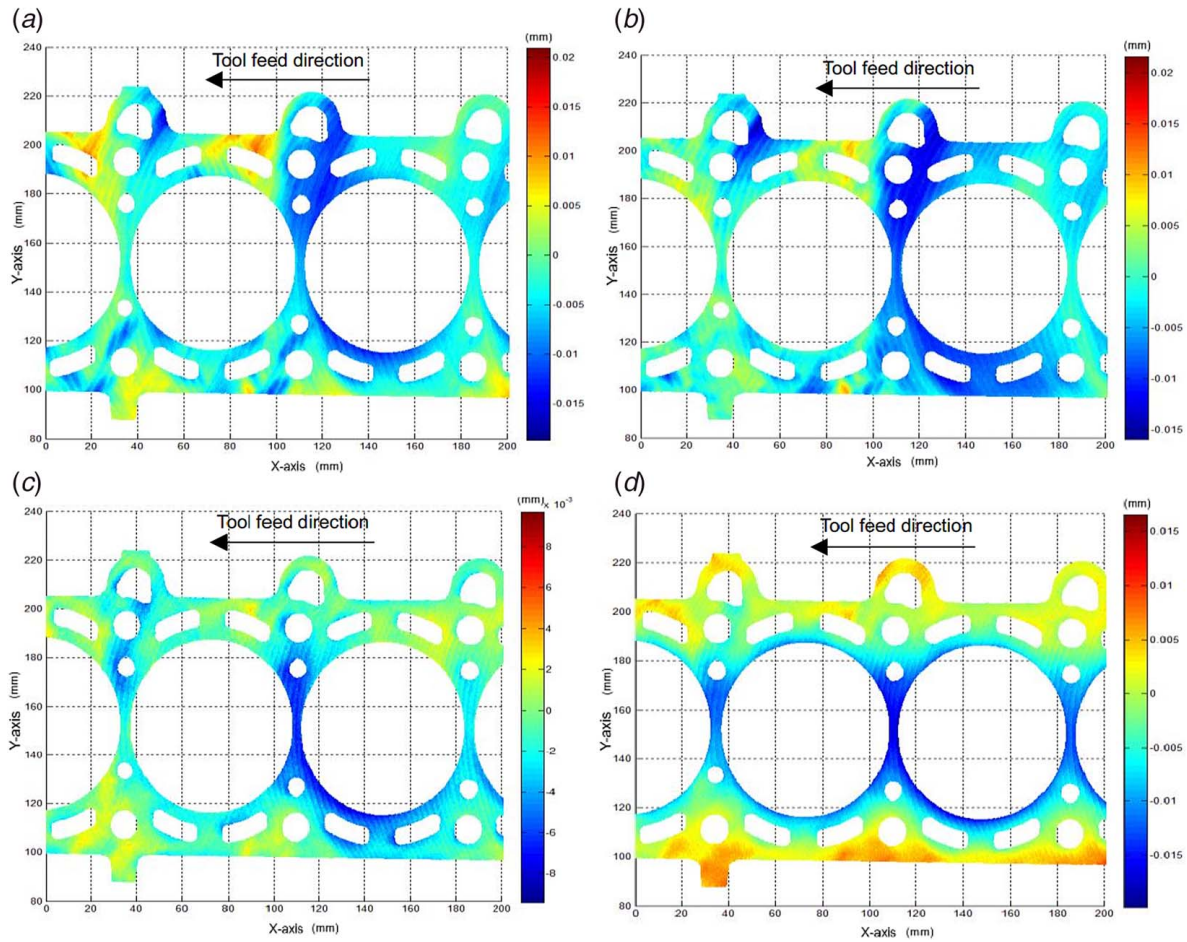

Fig. 28 HDM data transformed two-dimensional image: (*a*) data for case (1), (*b*) data for case (2), (*c*) data for case (3), and (*d*) data for case (4)

Table 4 Proposed evaluation indexes for different cases

	h_d			s_λ			h_f		
Index	Measured (μm)	Predicted (μm)	Error (%)	Measured (μm)	Predicted (μm)	Error (%)	Measured (μm)	Predicted (μm)	Error (%)
Case (1)	29.4	27.6	6.12	130.0	128.3	1.31	9.3	7.9	15.05
Case (2)	21.4	20.3	5.08	100.5	102.1	1.59	8.1	7.2	8.1
Case (3)	20.1	18.8	5.88	81.3	78.6	3.32	10.4	9.5	8.65
Case (4)	26.2	24.8	5.32	84.2	82.5	2.21	11.4	10.3	9.6

Table 5 ISO areal surface texture parameters for different cases

Case	S_q (μm)	S_p (μm)	S_v (μm)	S_z (μm)	S_a (μm)	S_{sk}	S_{ku}	S_{al}	S_{tr}
(1)	2.34	8.63	13.65	23.69	1.25	0.52	3.62	2.33	0.94
(2)	1.22	4.22	8.27	4.36	0.65	−0.13	1.33	1.59	0.41
(3)	0.98	5.36	7.37	10.81	0.49	0.36	1.03	1.64	0.33
(4)	1.58	6.32	10.04	12.56	0.78	0.44	1.68	1.87	0.63

4 Conclusion

A novel HDM-enabled approach for surface texture quality improvement is proposed in this research. The physical model for the face milling process of workpieces with discontinuous surfaces is constructed, comprehensively considering the effects of spindle tilt, tool conditions, and chatter stability. Three evaluation indexes are defined based on the HDM data in particular for surface texture with tool marks, which can be quantitatively predicted by the proposed physical model. Taking these evaluation indexes as the objectives, this research provides a physics-informed optimization model to optimize the processing parameters for improving the face milled surface quality. To validate the effectiveness of the proposed approach, a series of face milling experiments are conducted on a typical type of four-cylinder engine blocks. Tool conditions including insert runouts and tool wear are measured, respectively. The machined surfaces are measured by the HDM instruments to obtain high resolution data of surface texture. The theoretical calculation results of evaluation indexes based on the proposed physical model are in good agreement with the measurement results, indicating that the proposed approach can accurately predict the surface texture quality. Moreover, according to the evaluation indexes as well as the ISO standard parameters, calculated based on the measured HDM data, the quality of surface texture is significantly improved by utilizing the optimized processing parameters.

For future work, more inner factors that affect surface texture quality such as residual stress and heat-induced surface hardening should be taken into consideration, aimed at improving accuracy and generality of the physical model.

Acknowledgment

This work is supported by the National Natural Science Foundation of China (Grant No. 51775343) and sponsored by Shanghai Pujiang Program (Grant No. 18PJC031). The authors sincerely thank Shanghai Automotive Industry Corporation General Motors Wuling Company in Liuzhou, China, for providing the engine blocks for experiments.

Conflict of Interest

There are no conflicts of interest.

Data Availability Statement

The datasets generated and supporting the findings of this article are obtainable from the corresponding author upon reasonable request. The authors attest that all data for this study are included in the paper. Data provided by a third party listed in Acknowledgment. No data, models, or code were generated or used for this paper.

Nomenclature

f = feed rate (mm/min)
N = total number of inserts
R = ideal cutter radius (mm)
a_e = radial cutting depth (mm)
a_p = axial cutting depth (mm)
a_{p_lim} = critical axial cutting depth (mm)
f_z = feed per insert (mm)
h_d = average peak-valley difference (mm)
h_f = height fluctuation (mm)
h_i = general height wear of wiper edge on insert i (mm)
k_L = serial number of stability lobes
s_λ = wavelength spacing (mm)
t_c = cutting duration (s)
t_{uc} = thickness of undeformed chip (mm)
K_t = tangential cutting coefficient
L_c = cutting distance (mm)
N_e = number of inserts engaged with workpiece
R_I = corrected cutter radius (mm)
N^* = maximum number of inserts
α = intersection angle between general cutting edge and wiper edge (deg)
β_i = rotational runout of insert i (deg)
ε_{ai} = axial runout of insert i (mm)
ε_{ri} = radial runout of insert i (mm)
ϕ = lead angle of insert (deg)
ϕ_a = actual lead angle of insert (deg)
ϕ_0 = spindle inclination (deg)
κ = angle difference between two adjacent inserts (deg)
λ_f = cutoff wavelength for filtering (mm)
Λ_I = imaginary part of the eigenvalue
Λ_R = real part of the eigenvalue
ω_c = chatter frequency (Hz)
Ω = spindle speed (rpm)

Appendix A

The general height wear of the wiper edge h_i can be generated by the following steps.

Step 1: Check if the wiper edge of insert i is worn. If so, proceed to Step 2; if not, $h_i = 0$ and the program is ended.
Step 2: Initialization by setting $B_i = 1$ and $h_i = 0$.
Step 3: By continuously enlarging h_i till $h_i = H_i$, update h_i with the current value and set $B_i = B_i + 1$ once a new intersect is generated by the wear edge curve and the function line $z = h_i$.
Step 4: The program is ended when $h_i = H_i$.

Appendix B

Denoting the identity matrix by $[I]$, the characteristic equation of regenerative chatter is given by

$$\det\{[I]-\frac{2\pi\Lambda}{N_e}[G(i\omega_c)]\}=0 \tag{B1}$$

Therein, Λ is the eigenvalue and formulated by

$$\Lambda=\frac{N}{4\pi}a_p K_t(1-e^{-i\omega_c\tau}) \tag{B2}$$

where τ is the insert passing period given by $\tau=60/\Omega N$, while e is the base of natural logarithm and approximately equals to 2.718 in this research.

Evidently Λ is a complex number and thus can be rewritten as the sum of real part and imaginary part, namely, $\Lambda=\Lambda_R+i\Lambda_I$. By utilizing the Euler's formula [64], Λ_R and Λ_I can be calculated by

$$\begin{cases}\Lambda_R=\dfrac{N}{4\pi}a_p K_t(1-\cos(\omega_c\tau))\\ \Lambda_I=\dfrac{N}{4\pi}a_p K_t\sin(\omega_c\tau)\end{cases} \tag{B3}$$

And Eq. (B3) can be further derived as

$$\frac{\Lambda_I}{\Lambda_R}=\frac{\sin(\omega_c\tau)}{1-\cos(\omega_c\tau)} \tag{B4}$$

References

[1] Dong, W. P., Sullivan, P. J., and Stout, K. J., 1992, "Comprehensive Study of Parameters for Characterizing 3D Surface Topography I: Some Inherent Properties of Parameter Variation," Wear, **159**(2), pp. 161–171.

[2] Wang, B., Dong, X., Wang, Z., Wang, Y., and Hou, Z., 2020, "The Humidity-Induced Sensitivity Amplification Effect in an Ionization Gas Sensor With Silicon Nanostructures," IEEE Electron Device Lett., **41**(6), pp. 908–911.

[3] Ryu, S. H., Choi, D. K., and Chu, C. N., 2006, "Roughness and Texture Generation on End Milled Surfaces," Int. J. Mach. Tools Manuf., **46**(3–4), pp. 404–412.

[4] Thompson, R. A., 1992, "On the Doubly Regenerative Stability of a Grinder: The Effect of Contact Stiffness and Wave Filtering," ASME J. Manuf. Sci. Eng., **114**(1), pp. 53–60 .

[5] Mohandesi, J. A., Rafiee, M. A., Maffi, O., and Saffarzadeh, P., 2007, "Dependence of the Yield and Fatigue Strength of the Thread Rolled Mild Steel on Dislocation Density," ASME J. Manuf. Sci. Eng., **129**(1), pp. 216–222.

[6] Mohammadtabar, N., Bakhshi-Jooybari, M., Gorji, H., Jamaati, R., and Szpunar, J. A., 2021, "Effect of Electric Current Pulse Type on Springback, Microstructure, Texture, and Mechanical Properties During V-Bending of AA2024 Aluminum Alloy," ASME J. Manuf. Sci. Eng., **143**(1), p. 011004.

[7] Yoo, S., and Walczyk, D. F., 2007, "A Preliminary Study of Sealing and Heat Transfer Performance of Conformal Channels and Cooling Fins in Laminated Tooling," ASME J. Manuf. Sci. Eng., **129**(2), pp. 388–399.

[8] Wang, K., Li, G., Du, S., Xi, L., and Xia, T., 2021, "State Space Modelling of Variation Propagation in Multistage Machining Processes for Variable Stiffness Structure Workpieces," Int. J. Prod. Res., **59**(13), pp. 4033–4052.

[9] Blunt, L., and Stout, K. J., 2000, *Three-Dimensional Surface Topography*, Penton, London.

[10] Li, G., Du, S., Huang, D., Zhao, C., and Deng, Y., 2019, "Elastic Mechanics-Based Fixturing Scheme Optimization of Variable Stiffness Structure Workpieces for Surface Quality Improvement," Precis. Eng., **56**, pp. 343–363.

[11] Villa, A., Rossetto, S., and Levi, R., 1983, "Surface Texture and Machining Conditions. Part 1: Model Building Logic in View of Process Control," ASME J. Eng. Ind., **105**(4), pp. 259–263.

[12] Villa, A., Rossetto, S., and Levi, R., 1983, "Surface Texture and Machining Conditions. Part 2: Development of Mathematical Model Based Upon Pattern Recognition," ASME J. Eng. Ind., **105**(4), pp. 264–269.

[13] Hadad, M., and Ramezani, M., 2016, "Modeling and Analysis of a Novel Approach in Machining and Structuring of Flat Surfaces Using Face Milling Process," Int. J. Mach. Tools Manuf., **105**, pp. 32–44.

[14] Salisbury, E. J., Domala, K. V., Moon, K. S., Miller, M. H., and Sutherland, J. W., 2001, "A Three-Dimensional Model for the Surface Texture in Surface Grinding, Part 1: Surface Generation Model," ASME J. Manuf. Sci. Eng., **123**(4), pp. 576–581.

[15] Salisbury, E. J., Domala, K. V., Moon, K. S., Miller, M. H., and Sutherland, J. W., 2001, "A Three-Dimensional Model for the Surface Texture in Surface Grinding, Part 2: Grinding Wheel Surface Texture Model," ASME J. Manuf. Sci. Eng., **123**(4), pp. 582–590.

[16] Baek, D. K., Ko, T. J., and Kim, H. S., 1997, "A Dynamic Surface Roughness Model for Face Milling," Precis. Eng., **20**(3), pp. 171–178.

[17] Kiss, A. K., Bachrathy, D., and Stepan, G., 2020, "Effects of Varying Dynamics of Flexible Workpieces in Milling Operations," ASME J. Manuf. Sci. Eng., **142**(1), p. 011005.

[18] Shen, J., Xu, P., and Yu, Y., 2020, "Dynamic Characteristics Analysis and Finite Element Simulation of Steel-BFPC Machine Tool Joint Surface," ASME J. Manuf. Sci. Eng., **142**(1), p. 011006.

[19] Batsch, M., 2020, "A Novel Method of Obtaining Honing Tool Profile for Machining Gears With Profile Modifications," ASME J. Manuf. Sci. Eng., **142**(9), p. 091004.

[20] Du, S., and Xi, L., 2019, *High Definition Metrology Based Surface Quality Control and Applications*, Springer, Singapore.

[21] Du, S., Huang, D., and Wang, H., 2015, "An Adaptive Support Vector Machine-Based Workpiece Surface Classification System Using High Definition Metrology," IEEE Trans. Instrum. Meas., **64**(10), pp. 2590–2604.

[22] Huang, D., Du, S., Li, G., and Wu, Z., 2017, "A Systematic Approach for Online Minimizing Volume Difference of Multiple Chambers in Machining Processes Based on High-Definition Metrology," ASME J. Manuf. Sci. Eng., **139**(8), p. 081003.

[23] Huang, D., Du, S., Li, G., Zhao, C., and Deng, Y., 2018, "Detection and Monitoring of Defects on Three-Dimensional Curved Surfaces Based on High-Density Point Cloud Data," Precis. Eng., **53**, pp. 79–95.

[24] Du, S., Liu, T., Huang, D., and Li, G., 2018, "A Fast and Adaptive Bi-Dimensional Empirical Mode Decomposition Approach for Filtering of Workpiece Surfaces Using High Definition Metrology," J. Manuf. Syst., **46**, pp. 247–263.

[25] Shao, Y., Wang, K., Du, S., and Xi, L., 2018, "High Definition Metrology Enabled Three Dimensional Discontinuous Surface Filtering by Extended Tetrolet Transform," J. Manuf. Syst., **49**, pp. 75–92.

[26] Shi, J., Cao, H., Maroju, N. K., and Jin, X., 2020, "Dynamic Modeling of Aerostatic Spindle With Shaft Tilt Deformation," ASME J. Manuf. Sci. Eng., **142**(2), p. 021006.

[27] Li, J., Kilic, Z. M., and Altintas, Y., 2020, "General Cutting Dynamics Model for Five-Axis Ball-End Milling Operations," ASME J. Manuf. Sci. Eng., **142**(12), p. 121003.

[28] Yin, Y., Shao, Y., Wang, K., Du, S., and Xi, L., 2020, "Segmentation of Workpiece Surfaces With Tool Marks Based on High Definition Metrology," J. Manuf. Processes, **57**, pp. 268–287.

[29] Shao, Y., Yin, Y., Du, S., Xia, T., and Xi, L., 2018, "Leakage Monitoring in Static Sealing Interface Based on Three Dimensional Surface Topography Indicator," ASME J. Manuf. Sci. Eng., **140**(10), p. 101003.

[30] Ren, J., and Wang, H., 2018, "Surface Variation Modeling by Fusing Multi-Resolution Spatially Nonstationary Data Under a Transfer Learning Framework," ASME J. Manuf. Sci. Eng., **141**(1), p. 011002.

[31] Wang, B., Dong, X., Wang, Z., Wang, Y., and Hou, Z., 2020, "MEMS-Based Ionization Gas Sensors for VOCs With Array of Nanostructured Silicon Needles," ACS Sens., **5**(4), pp. 994–1101.

[32] Nguyen, H. T., Wang, H., and Hu, S. J., 2013, "Characterization of Cutting Force Induced Surface Shape Variation Using High-Definition Metrology," ASME J. Manuf. Sci. Eng., **135**(4), p. 041014.

[33] Lu, H. S., Chang, C. K., Hwang, N. C., and Chung, C. T., 2009, "Grey Relational Analysis Coupled With Principal Component Analysis for Optimization Design of the Cutting Parameters in High-Speed End Milling," J. Mater. Process. Technol., **209**(8), pp. 3808–3817.

[34] Mukherjee, I., and Ray, P. K., 2006, "A Review of Optimization Techniques in Metal Cutting Processes," Comput. Ind. Eng., **50**(1–2), pp. 15–34.

[35] Wang, H., Suriano, S., Zhou, L., and Hu, S. J., 2009, "High-Definition Metrology Based Spatial Variation Pattern Analysis for Machining Process Monitoring and Diagnosis," Proceedings of the ASME 2009 International Manufacturing Science and Engineering Conference, West Lafayette, IN, Oct. 4–7, Vol. 2, pp. 471–480.

[36] Suriano, S., Wang, H., and Hu, S. J., 2012, "Sequential Monitoring of Surface Spatial Variation in Automotive Machining Processes Based on High Definition Metrology," J. Manuf. Syst., **31**(1), pp. 8–14.

[37] Tai, B. L., Stephenson, D. A., and Shih, A. J., 2011, "Improvement of Surface Flatness in Face Milling Based on 3-D Holographic Laser Metrology," Int. J. Mach. Tools Manuf., **51**(6), pp. 483–490.

[38] Zhou, L., Wang, H., Berry, C., Weng, X., and Hu, S. J., 2011, "Functional Morphing in Multistage Manufacturing and Its Applications in High-Definition Metrology-Based Process Control," IEEE Trans. Autom. Sci. Eng., **9**(1), pp. 124–136 .

[39] Nguyen, H. T., Wang, H., and Hu, S. J., 2014, "Modeling Cutter Tilt and Cutter-Spindle Stiffness for Machine Condition Monitoring in Face Milling Using High-Definition Surface Metrology," Int. J. Adv. Manuf. Technol., **70**, pp. 1323–1335.

[40] Deb, K., Pratap A., Agarwal S., and Meyarivan, T., 2002, "A Fast and Elitist Multiobjective Genetic Algorithm: NSGA-II," IEEE Trans. Evol. Comput., **6**(2), pp. 182–197.

[41] Li, H., and Zhang, Q., 2009, "Multiobjective Optimization Problems With Complicated Pareto Sets, MOEA/D and NSGA-II," IEEE Trans. Evol. Comput., **13**(2), pp. 284–302.

[42] Liu, Q., Tian, Y., Wang, C., Chekem, F. O., and Sutherland, J., 2018, "Flexible Job-Shop Scheduling for Reduced Manufacturing Carbon Footprint," ASME J. Manuf. Sci. Eng., **140**(6), p. 061006.

[43] ISO, 2015, "Geometrical Product Specifications (GPS)-Filtration Part 61: Linear Areal Filters: Gaussian Filters," International Organization for Standardization, Geneva, Switzerland, Standard No. ISO 16610-61:2015 .

[44] Wang, M., Ken, T., Du, S., and Xi, L., 2015, "Tool Wear Monitoring of Wiper Inserts in Multi-Insert Face Milling Using Three-Dimensional Surface Form Indicators," ASME J. Manuf. Sci. Eng., **137**(3), p. 031006.

[45] ISO, 2012, "Geometrical Product Specifications (GPS)-Surface Texture: Areal Part 2: Terms, Definitions and Surface Texture Parameters," International Organization for Standardization, Geneva, Switzerland, Standard No. ISO 25178-2:2012 .
[46] ISO, 2015, "Geometrical Product Specifications (GPS)-Filtration Part 40: Morphological Profile Filters: Basic Concepts," International Organization for Standardization, Geneva, Switzerland, Standard No. ISO 16610-40:2015 .
[47] ISO, 2015, "Geometrical Product Specifications (GPS)-Filtration Part 85: Morphological Areal Filters: Segmentation," International Organization for Standardization, Geneva, Switzerland, Standard No. ISO 16610-85:2015 .
[48] Schmitz, T. L., Couey, J., Marshb, E., Mauntler, N., and Hughes, D., 2006, "Runout Effects in Milling: Surface Finish, Surface Location Error and Stability," Int. J. Mach. Tools Manuf., **47**(5), pp. 841–851.
[49] Kline, W. A., and Devor, R. E., 1983, "The Effect of Runout on Cutting Geometry and Forces in End Milling," Int. J. Mach. Tool Des. Res., **23**(2–3), pp. 123–140.
[50] Smith, G. T., 2008, *Cutting Tool Technology Industrial Handbook*, Springer, London.
[51] Liu, S., Jin, S., Zhang, X., Chen, K., Tian, A., and Xi, L., 2019, "A Coupled Model for the Prediction of Surface Variation in Face Milling Large-Scale Workpiece With Complex Geometry," ASME J. Manuf. Sci. Eng., **141**(3), p. 031009.
[52] Stephenson, D. A., and Agapiou, J. S., 1997, *Metal Cutting Theory and Practice Manufacturing*, CRC Press, New York.
[53] Liao, Y., Stephenson, D. A., and Ni, J., 2010, "A Multifeature Approach to Tool Wear Estimation Using 3D Workpiece Surface Texture Parameters," ASME J. Manuf. Sci. Eng., **132**(6), p. 061008.
[54] Smith, S., and Tlusty, J., 1993, "Efficient Simulation Programs for Chatter in Milling," CIRP Ann., **42**(1), pp. 463–466.
[55] Eksioglu, C., Kilic, Z. M., and Altintas, Y., 2012, "Discrete-Time Prediction of Chatter Stability, Cutting Forces, and Surface Location Errors in Flexible Milling Systems," ASME J. Manuf. Sci. Eng., **134**(6), p. 061006.
[56] Ding, Y., Zhu, L., Zhang, X., and Ding, H., 2010, "A Full-Discretization Method for Prediction of Milling Stability," Int. J. Mach. Tool Manuf., **50**(5), pp. 502–509.
[57] Wan, M., Pan, W.-J., Zhang, W.-H., Ma, Y.-C., and Yang, Y., 2014, "A Unified Instantaneous Cutting Force Model for Flat End Mills With Variable Geometries," J. Mater. Process. Technol., **214**(3), pp. 641–650.
[58] Li, G., Du, S., Huang, D., Zhao, C., and Deng, Y., 2019, "Dynamics Modeling-Based Optimization of Process Parameters in Face Milling of Workpieces With Discontinuous Surfaces," ASME J. Manuf. Sci. Eng., **141**(10), p. 101009.
[59] Cao, H., Li, B., and He, Z., 2012, "Chatter Stability of Milling With Speed-Varying Dynamics of Spindles," Int. J. Mach. Tool Manuf., **52**(1), pp. 50–58.
[60] Zain, A. M., Haron, H., and Sharif, S., 2010, "Prediction of Surface Roughness in the End Milling Machining Using Artificial Neural Network," Expert Syst. Appl., **37**(2), pp. 1755–1768.
[61] Vivancos, J., Luis, C., Costa, L., and Ortiz, J., 2004, "Optimal Machining Parameters Selection in High Speed Milling of Hardened Steels for Injection Moulds," J. Mater. Process. Technol., **155**(1), pp. 1505–1512.
[62] Franco, P., Estrems, M., and Faura, F., 2008, "A Study of Back Cutting Surface Finish From Tool Errors and Machine Tool Deviations During Face Milling," Int. J. Mach. Tools Manuf., **48**(1), pp. 112–123.
[63] Franco, P., Estrems, M., and Faura, F., 2004, "Influence of Radial and Axial Runouts on Surface Roughness in Face Milling With Round Insert Cutting Tools," Int. J. Mach. Tools Manuf., **44**(15), pp. 1555–1565.
[64] Svetlik, M., Radojicic, M., Radovic, S., and Simic-Muller, K., 2018, "Justifying Euler's Formula Through Motion in a Plane," Math. Enthus., **15**(3), pp. 397–406.